Response to Referee 1:

Referee 1:

The manuscript by P. S. Tarabunga and T. Haug provides a comprehensive study to different magic diagnostic for the quantum many-body physics. The pros are that they explain in details each definition of the diagnostic, but the cons are that these different quantities are not well organized in a coherent logical flow, and the demonstration of the methods needs to be improved. Overall, their computation methods could benefit the community, but the current presented version of the manuscript is not yet ready for publication in SciPost. My detailed comments / suggestions are as follows:

Response: We thank the Referee for their careful evaluation of the manuscript, and for recognizing that our work could benefit the community on the study of magic. Below we address the Referee's constructive comments.

Referee 1:

1. Parallel definitions of the distribution functions and entropies: In Sec III, their Eq.6-8 are alternative definitions of the SRE based on an alternative distribution function $q = tr(\rho P \rho P)/2^N$, in comparison with $p = tr(\rho P)^2/tr(\rho^2)/2^N$ in Eq.3-4 of Sec II. They should both be placed in Sec II, before introducing the finer quantities of mutual magic and magic capacity. After all, the probability distribution is the basic of everything that follows.

Response: We now define the alternative distribution q_ρ in Sec. II.

Referee 1:

2. Motivation for the alternative distribution: They should explain earlier the motivation why they need to introduce a different distribution q, otherwise it is very confusing – in principle one can define a lot of different distribution functions from a quantum state. I did not understand their motivation until reading their paragraph following Eq.17-18 in Sec IV – is it simply because such definition saves the computation of mutual magic by roughly a factor 3 (since one does not need to evaluate A and B separately)?

Response: The distribution p_ρ appears to be the most natural extension from pure states, as it is obtained simply by normalizing the distribution for pure states. This is in fact the approach that was taken in the previous definition of mixed-state SRE in Leone *et al.* (2022). We introduce the alternative distribution q_ρ because it has a nice property that, for any subsystem A, the distribution for the reduced density matrix $\rho_A = tr_{A^c}(\rho)$ is simply the marginal distribution of q_ρ in A. We added a proof of this property in Appendix A. This property gives a clear relation between the mutual magic defined based on q_ρ and the (classical) mutual information of q_ρ. Moreover, it provides a substantial practical advantage in the perfect sampling approach for computing the mutual magic. As the Referee correctly noted, this property eliminates the need to separately compute the SREs for subsystems A and B, as it allows the mutual SRE to be estimated by sampling only the full q_ρ distribution. However, we note that the improvement goes beyond this factor of 3 saving. In fact, the estimation of $\mathcal{I}_1^{[q]}$ is expected to require significantly fewer samples than $\mathcal{I}_1^{[p]}$ because it avoids the need to accurately estimate the individual SREs for the

subsystems. We corroborate this computational advantage with our numerical results for the transverse-field Ising model, as detailed in Appendix B. We found that achieving comparable data quality required us to use $K = 2 \times 10^6$ Pauli samples to estimate $\mathcal{I}_1^{[p]}$, while only $K = 10^5$ samples were needed for $\mathcal{I}_1^{[q]}$.

We have revised our manuscript to stress these points, in particular in Sec. II, Sec. IIIA, and Sec. IVA.

Referee 1:

> 3. I'm a bit confused what purpose Fig.1 serves? It is embedded in Sec IV explaining methods. But Fig.1a (with its caption and texts in paragraphs) does not tell us the efficiency and accuracy neither the physical implication of the anisotropic Heisenberg ground state. Fig.1b and its texts only tell us the convergence of small bond dimension MPS methods, and Monte Carlo based on finite bond dimension as well.

Response: The purpose of Fig.1 is to illustrate the new Monte Carlo methods we propose in Sec. IVB, rather than to uncover a new behavior. For Fig. 1a, we have added an observation that the statistical errors significantly increase as the anisotropy approaches $\Delta = 1$. This is connected to our analysis that the efficiency of the method is dictated by the anti-flatness of Pauli spectrum (see Eq. (28) and the discussion after). As we subsequently show in Sec. V, the magic capacity C_M, which measures the anti-flatness, has a drastic increase (and even change of scaling with N) as the anisotropy approaches $\Delta = 1$.

Fig. 1b tells us that the method of approximating the prior $\Pi(P)$ with another prior $\tilde{\Pi}(P)$ constructed from smaller bond dimension MPS can produce accurate results. In particular, it can be seen that the Monte Carlo results are indistinguishable from the exact contraction with $\chi = 8$.

Referee 1:

> 4. Sec. V-A, Clifford + T circuit physics: in their Fig.2b, the data is noisy, and there is too limited number of data points near the suspicious "crossing point", which is far from convincing that the observable scales large for $z < z_c$ and scales to 0 for $z > z_c$. Similarly for the data at $z > z_c$ in Fig.2c. It is hard to claim "critical point(s)" based on the existing data presentation in Fig.2bc. For Fig.2a, what "(entanglement/magic/information) order parameter" can distinguish the two phases if this is a "transition"?

Response: We thank the referee for the comment. We want to show how magic or C_M saturates its maximal value. This is essential to understand how stabilizer states (which have zero magic) become Haar (which have maximal magic) by injecting T-gates, which is known to happen for sufficiently many T-gates, but the exact number of T-gates is not known. By using SRE or magic capacity, we can lower bound this transition to Haar randomness. In particular, it is known that Clifford+T circuits saturate the maximal SRE M_α in a sharp transition for large N. Such a saturation transitions appear at a critical $z_{c,\alpha}$, which depends on the chosen α of the α-SRE Haug *et al.* (2025). This saturation transition is characterized by a universal behavior of $\partial_z m_\alpha$, where $m_\alpha = M_\alpha/N$ is the magic density and ∂_z is the derivative with respect to z. In particular, one finds that the curves of $\partial_z m_\alpha$ for different N cross at the same $z_{c,\alpha}$. Further, by a proper rescaling, $\partial_z m_\alpha(N)$ can be made to collapse to a single curve for all N Haug *et al.* (2025). This is hallmark of universal behavior, often found in phase transitions (e.g. previously

found for entanglement at critical points of the Ising model), where the properties of the system become scale-invariant and simple functions of N Osterloh *et al.* (2002).

To enhance our study, we gathered more samples, which significantly reduced the noise on the data. We also added more plots, splitting the discussion of M_1 into Fig. 2 and C_M into Fig.3 The saturation transition, where curves for different N meet, is now clearly visible in Fig.2b, showing that the saturation transition happens at $z_{c,1} \approx 2.05$. We added Fig.2c to show that when properly rescaling, the derivative $\partial_z m_1$ can be made to collapse into a single curve for any N. This is hallmark feature of universality, showing that the behavior is a simple function of N, usually found at critical points.

Similarly, we find such saturation transition for C_M, however at a different point $z_{c,C_M} \approx 2.35$. Beyond the transition, C_M assumes its value expected for Haar random states. In Fig.3a, we find such a transition for C_M, where curves meet for all N. Similarly, in the new Fig.3c, we find also a crossing at the same point for $\partial_z C_M/N$. Close to the transition, we can collapse the curves for different N, which we show in the new Fig.3d. Note that due to finite size effects, we observe the transition only for $N \geq 12$.

Referee 1:

> 5. Sec. V-B, in Fig.3 anisotropic Heisenberg chain ground state: this is a paradig-
> matic integrable model with very rich analytic and numerical understanding in the
> literature, concerning its universal features in long-wave-length limit. The magic
> calculation is new – can the authors elucidate what known or unknown universal
> scaling exponents can be extracted from the magic quantities they calculate? If they
> go to stronger anisotropic coupling to gap out the gapless quantum chain, what do
> they observe in the magic quantities? Can they tell the phase transition?

Response: We thank the referee for these interesting questions. However, the main objective of our work is to introduce and demonstrate a new class of efficiently computable magic quantities. The purpose of our numerical results is to showcase the utility of these quantities in various settings, not to perform an exhaustive study on specific models. In particular, for the anisotropic Heisenberg chain, we find an interesting behavior where the magic capacity C_M changes its scaling with N as the anisotropy approaches $\Delta = 1$. This contrasts with the SREs, which do not show this behavior. We hope that this interesting finding will inspire future studies on a more detailed analysis of magic behavior in the Heisenberg chain.

Referee 1:

> 6. Fig.4-5 for TFIM – can they show the data collapse? Without the prior knowl-
> edge of the exact solution $h_c = 1$, what numerical h_c can they get? Which scaling
> operators are responsible for the scaling of 1-SRE and 2-SRE here?

Response: We study the collapse for $\mathcal{I}_2$ in more detail in the Appendix in Fig.S6. We added Fig. S6d, where we show how the minimal field $h_0(N)$ of M_2 found for every N is plotted against N. By fitting with a polynomial, we find that $h_0(N)$ for $N \to \infty$ converges to $h_c^{\text{fit}} \approx 1.004$, which is close to the analytic value of $h_c = 1$.

We adopt our fitting procedure for m_1, C_M, $\mathcal{I}_2$ and $\mathcal{I}_1^{[q]}$ in the new Appendix G. We find that by fitting the extremal values of those properties, we can find the critical field with high precision.

Regarding scaling operators, since our work does not focus on field theory, we will simply refer to Refs. Hoshino *et al.* (2025); Hoshino and Ashida (2025) which have performed con-

formal field theory (CFT) calculations on the SRE. The CFT calculations for the new quantities that we introduced is an interesting avenue that we leave for future studies.

References

L. Leone, S. F. E. Oliviero, and A. Hamma, Phys. Rev. Lett. **128**, 050402 (2022).

T. Haug, L. Aolita, and M. Kim, Quantum **9**, 1801 (2025).

A. Osterloh, L. Amico, G. Falci, and R. Fazio, Nature **416**, 608 (2002).

M. Hoshino, M. Oshikawa, and Y. Ashida, arxiv:2503.13599 (2025).

M. Hoshino and Y. Ashida, arxiv:2507.10656 (2025).

Efficient mutual magic and magic capacity with matrix product states

Poetri Sonya Tarabunga[1, 2, *] and Tobias Haug[3, †]

[1] *Technical University of Munich, TUM School of Natural Sciences, Physics Department, 85748 Garching, Germany*
[2] *Munich Center for Quantum Science and Technology (MCQST), Schellingstr. 4, 80799 München, Germany*
[3] *Quantum Research Center, Technology Innovation Institute, Abu Dhabi, UAE*

Stabilizer Rényi entropies (SREs) probe the non-stabilizerness (or 'magic') of many-body systems and quantum computers. Here, we introduce the mutual von-Neumann SRE and magic capacity, which can be efficiently computed in time $O(N\chi^3)$ for matrix product states (MPSs) of bond dimension χ. We find that mutual SRE characterizes the critical point of ground states of the transverse-field Ising model, independently of the chosen local basis. Then, we relate the magic capacity to the anti-flatness of the Pauli spectrum, which quantifies the complexity of computing SREs. The magic capacity characterizes transitions in the ground state of the Heisenberg and Ising model, randomness of Clifford+T circuits, and distinguishes typical and atypical states. Finally, we make progress on numerical techniques: we design two improved Monte-Carlo algorithms to compute the mutual 2-SRE, overcoming limitations of previous approaches based on local update. We also give improved statevector simulation methods for Bell sampling and SREs with $O(8^{N/2})$ time and $O(2^N)$ memory, which we demonstrate for 24 qubits. Our work uncovers improved approaches to study the complexity of quantum many-body systems.

I. INTRODUCTION

Nonstabilizerness, also known as magic, is recognized as a key resource for quantum computing and a necessary condition for demonstrating quantum advantage [1, 2]. It is based on the notion of stabilizer states [3], which are those generated by Clifford unitary operators and which play a key role in quantum computation and error correction [4–6].

Essentially, nonstabilizerness quantifies the degree to which a quantum state cannot be approximated by a stabilizer state. Given that stabilizer states are efficiently simulable classically [7–9], nonstabilizerness determines the minimal non-Clifford resources required for universal quantum computation [5, 6]. It also provides a lower bound on these resources and is indicative of the complexity of classical simulation algorithms using techniques based on the stabilizer formalism [2, 10]. Consequently, the quantitative characterization of nonstabilizerness, especially in many-body contexts, is of paramount importance.

Several measures of magic have been proposed in quantum information theory, such as the min-relative entropy of magic [11, 12], the relative entropy of magic [2], the robustness of magic [12, 13], and the basis-minimized stabilizerness asymmetry [14]. However, the computation of these measures involve complex minimization procedures, making their computation a significant challenge in many-body systems. To address this problem, stabilizer Rényi entropies (SREs) [15] were introduced, providing efficiently accessible magic measures for both numerical [16–23] and experimental studies [24–28]. SREs have found importance in many-body phenomena [12],

such as phase transitions [16, 19, 21, 23, 29–32], quantum chaos [33–37], quantum dynamics [38–41], transition in monitored circuits [42–44], and the structure of entanglement [45–50].

In addition to the study of magic in the full state, recently there has been a growing interest in the characterization of more refined aspects of magic. In particular, there has been substantial interest in nonlocal magic, which represents the nonstabilizerness that resides within the correlations between the subsystems [19, 44, 51–58]. Although nonlocal magic is ideally defined using a mixed-state magic monotone, the mutual 2-SRE [19] has been hypothesized to capture some form of nonlocal magic. While the SRE is not a proper magic monotone for mixed states, it can be used to construct mixed state magic witness [28]. Notably, in some cases the mutual 2-SRE was found to display the same behavior as the mutual magic defined using genuine mixed state magic monotones [44]. It is also appealing because it is relatively easier to compute, allowing for numerical [19, 47, 48] and analytical [59, 60] studies of nonlocal magic in many-body quantum systems, particularly by applying tensor network methods. As the name suggests, the definition of mutual 2-SRE is directly reminiscent of mutual information of entanglement, and is thus expected to be free from UV divergences from the point of view of field theory [60]. Its connection to physical phenomena has also been revealed [19, 44, 48, 59, 60].

However, the mutual 2-SRE is still relatively expensive to compute for matrix product states (MPS), with the exact calculation scaling as $O(N\chi^{12})$ [16], where χ is the bond dimension of the MPS. Approximate contraction schemes and sampling-based techniques have also been proposed [19, 20, 61], with the latter mainly relying on Monte Carlo algorithms with local update rules. However, their convergence is not guaranteed, and their applicability needs to be tailored to the specific model under consideration. Overall, the existing approaches still

---

* poetri.tarabunga@tum.de
† tobias.haug@u.nus.edu

face limitations in their general applicability and computational efficiency.

Here, we present an efficient characterization of various magic properties. First, we introduce the mutual von-Neumann SRE to characterize nonlocal magic where we find two possible definitions. For MPS, the mutual von-Neumann SRE can be efficiently calculated via perfect sampling in $O(N\chi^3)$ time, where χ is the bond dimension and N the number of qubits. Additionally, we provide two new algorithms to compute the mutual 2-SRE based on Metropolis-Hastings Monte-Carlo. We show that mutual SREs are able to characterize the critical point of the transverse field Ising model (TFIM) in arbitrary local basis, overcoming the limitation of the bare SRE.

Further, we introduce the magic capacity C_M in analogy to the entanglement capacity [62], and show that it is connected to the anti-flatness of the Pauli spectrum. We efficiently compute the capacity of magic for MPS in $O(N\chi^3)$ time, and show that it describes the sampling complexity to compute the von-Neumann SRE. We find that phases in Clifford+T circuits as well the ground state of the Heisenberg model are characterized by the scaling of the magic capacity with N. Notably, we find that magic capacity provides an efficient tool to discriminate between typical and atypical states.

Finally, we provide an improved algorithm to perform Pauli and Bell sampling, which we apply to compute the von-Neumann SRE and magic capacity for statevector simulations of arbitrary states. Our method scales as $O(8^{N/2})$ time and $O(2^N)$ memory (in contrast to naive sampling with $O(8^N)$ time and $O(4^N)$ memory) allow simulation of at least 24 qubits. Our work enhances the characterization of different aspects of magic of many-body quantum systems and quantum circuits.

The rest of the paper is structured as follows. We define general α-SREs for mixed states in Sec. II. Next, we introduce the mutual von-Neumann SRE and magic capacity in Sec. III. In Sec. IV, we describe efficient numerical methods based on Pauli sampling, both for MPS and statevector simulations. In Sec. V, we present our numerical results on both Clifford+T circuits and ground state phase transitions. Finally, we discuss our results in Sec. VI. In Table I, we summarize the complexity of algorithms to compute SRE M_α, mutual α-SRE $\mathcal{I}_\alpha$ and magic capacity C_M for MPS, statevector simulation and quantum computers.

II. SRE

For N-qubit pure states $|\psi\rangle$, magic can be measured using the SRE [15], defined as

$$M_\alpha(|\psi\rangle) = H_\alpha[p_{|\psi\rangle}] - N\ln 2 =$$
$$\frac{1}{1-\alpha}\ln\left(2^{-N}\sum_{P\in\mathcal{P}_N}\langle\psi|P|\psi\rangle^{2\alpha}\right),$$

Index	Time
α-SRE M_α via MPS	
$\alpha = 1$	$O(N\chi^3 C_M \epsilon^{-2})$ [17, 18]
integer $\alpha > 1$	$O(N\chi^{6\alpha})$ [16]
Mutual α-SRE $\mathcal{I}_\alpha$ via MPS	
$\alpha = 1$	$O(N\chi^3 C_M \epsilon^{-2})$
$\alpha = 2$	$O(N\chi^{12})$ [19]
Magic capacity C_M via MPS	
C_M	$O(N\chi^3\epsilon^{-2})$
M_α and C_M via statevector simulation	
any α	$O(8^N)$ [15]
$\alpha = 1, C_M$	$O(8^{N/2}\epsilon^{-2})$

TABLE I. Complexity of computing SREs M_α and mutual SRE $\mathcal{I}_\alpha$ with Rényi index α, as well as magic capacity C_M. We consider algorithms for matrix product states (MPS) and statevector simulation. N is the number of qubits, χ is the bond dimension of matrix product state, ϵ the additive accuracy.

where $\mathcal{P}_N$ is the set of 4^N (unsigned) Pauli strings which are tensor products of single-qubit Pauli operators σ^x, σ^z, σ^y and identity I. Here, we use the α-Rényi entropy

$$H_\alpha[p] = \frac{1}{1-\alpha}\ln\left(\sum_p p^\alpha\right) \quad (1)$$

over the distribution of Pauli expectation values [15]

$$p_{|\psi\rangle}(P) = \frac{\langle\psi|P|\psi\rangle^2}{2^N}, \quad (2)$$

which satisfies $p_{|\psi\rangle} \geq 0$ and $\sum_{P\in\mathcal{P}_N} p_{|\psi\rangle}(P) = 1$. In the limit $\alpha \to 1$, one obtains the von-Neumann SRE [17, 18]

$$M_1(|\psi\rangle) = -2^{-N}\sum_{P\in\mathcal{P}_N}\langle\psi|P|\psi\rangle^2\ln\left(\langle\psi|P|\psi\rangle^2\right). \quad (3)$$

SREs have the following properties: i) For any pure stabilizer state $|\psi_C\rangle$, $M_\alpha(|\psi_C\rangle) = 0$, else $M_\alpha(|\psi\rangle) > 0$. ii) Invariant under Clifford unitaries U_C, i.e. $M_\alpha(U_C|\psi\rangle) = M_\alpha(|\psi\rangle)$, iii) Additive, i.e. $M_\alpha(|\psi\rangle \otimes |\phi\rangle) = M_\alpha(|\psi\rangle) + M_\alpha(|\phi\rangle)$. M_α is a monotone under channels that map pure states to pure states for $\alpha \geq 2$ [63], while this is not the case for $\alpha < 2$. Note that SREs are not strong monotones for any α [17], while they are for their linearized versions for $\alpha \geq 2$ [63].

In order to extend the SRE to mixed states, we need to generalize the probability distribution in Eq. (2). A modified distribution for mixed states can be constructed simply by adding a normalization factor, yielding

$$p_\rho(P) = 2^{-N}\frac{\text{tr}(\rho P)^2}{\text{tr}(\rho^2)}. \quad (4)$$

It is easy to see that $p_\rho \geq 0$ and $\sum_{P\in\mathcal{P}_N} p_\rho(P) = 1$. For pure states $p_{|\psi\rangle\langle\psi|} = p_{|\psi\rangle} = 2^{-N}\langle\psi|P|\psi\rangle^2$. We then

define the α-SREs for N-qubit mixed states ρ from the viewpoint of entropies as

$$\tilde{M}_\alpha(\rho) = H_\alpha(p_\rho) + S_2(\rho) - N\ln(2), \qquad (5)$$

where $S_2(\rho) = -\ln(\rho^2)$ is the 2-Rényi entropy. We note that the case $\alpha = 2$ is equivalent to the mixed-state SRE defined in Ref. [15]. If ρ describes a pure state, $\rho = |\psi\rangle\langle\psi|$, then we have $\tilde{M}_\alpha(\rho) = M_\alpha(|\psi\rangle)$.

For mixed states, $\tilde{M}_\alpha(\rho)$ is zero for mixed stabilizer states of the form $\rho_{C_0} = \sum_{P\in G}\alpha_P P$ (i.e. states that have a pure stabilizer state as their purification) where G is a commuting set of Pauli operators, and non-zero otherwise. However, states of the form of ρ_{C_0} are only a subset of all mixed stabilizer states, which are convex mixtures of pure stabilizer states $|\psi_C^{(i)}\rangle$, i.e. $\rho_C = \sum_i x_i |\psi_C^{(i)}\rangle\langle\psi_C^{(i)}|$. Thus, for mixed states $\tilde{M}_\alpha(\rho)$ is not a proper magic monotone. Nevertheless, it has a nice property of being efficiently computable, allowing us to probe magic in subsystems of many-body states.

While the distribution p_ρ appears to be the most natural extension, we will also consider an alternative probability distribution over Pauli strings P as

$$q_\rho(P) = 2^{-N}\mathrm{tr}(\rho P\rho P). \qquad (6)$$

Note that this distribution is closely related to Bell sampling, which samples from $P \sim 2^{-N}\mathrm{tr}(\rho^* P\rho P)$ [24, 64]. It is easy to see that $q_\rho(P) \geq 0$ due to $\rho \succeq 0$ and $P\rho P \succeq 0$. Further, we have $\sum_{P\in\mathcal{P}_N} q_\rho(P) = 1$ due to $\sum_{P\in\mathcal{P}_N} P\rho P = 2^N\mathrm{tr}(\rho)I_n$ where I_n is the identity. For pure states $q_{|\psi\rangle\langle\psi|} = p_{|\psi\rangle} = 2^{-N}\langle\psi|P|\psi\rangle^2$. A nice property of the distribution q_ρ is that, for any subsystem A, the distribution for the reduced density matrix $\rho_A = \mathrm{tr}_{A^c}(\rho)$ is simply the marginal distribution of q_ρ in A. In other words,

$$q_{\rho_A}(P_A) = \sum_{P\in\mathcal{P}_{A^c}} q_\rho(P_A \otimes P) \qquad (7)$$

for any $P_A \in \mathcal{P}_A$, which is proven in Appendix A. Here, given a subsystem A with N_A sites, $\mathcal{P}_A$ is the set of 4^{N_A} unsigned Pauli strings which consists of identities for any sites in the complement subsystem A^c. The property in Eq. (7) is particularly useful for computing the mutual SRE, which will be defined in Sec. III A. Note that the distribution p_ρ does not possess an analogous property.

One can now also define mixed-state SREs using q_ρ. For $\alpha = 2$, this conincides with $\tilde{M}_2$, i.e.

$$\tilde{M}_2^{[q]}(\rho) = H_2[q_\rho] - S_2(\rho) - N\ln(2) \equiv \tilde{M}_2(\rho) \qquad (8)$$

However, for $\alpha = 1$ one gains an alternate von-Neumann SRE

$$\tilde{M}_1^{[q]}(\rho) = H_1[q_\rho] - S_2(\rho) - N\ln(2). \qquad (9)$$

where $\tilde{M}_1^{[q]} \neq \tilde{M}_1$ and $H_1[q] = -\sum_q q\ln(q)$. One can show that $\tilde{M}_1^{[q]}$ has the same properties as $\tilde{M}_1$, which one can show using $\tilde{M}_1^{[q]} \geq \tilde{M}_2 \geq 0$ from the hierarchy of Rényi entropies, and $\tilde{M}_1^{[q]}(\rho_C) = 0$.

III. MUTUAL MAGIC AND MAGIC CAPACITY

In this section, we introduce new magic quantities, including mutual α-SRE $\mathcal{I}_\alpha$, an alternate definition of mutual von-Neumann SRE $\mathcal{I}_1^{[q]}$ and magic capacity C_M. We discuss how these quantities probe different aspects of magic. We will then show in the following sections that these quantities are efficiently computable with matrix product states.

A. Mutual SRE

We define mutual α-SREs as

$$\mathcal{I}_\alpha(\rho) = \tilde{M}_\alpha(\rho) - \tilde{M}_\alpha(\rho_B) - \tilde{M}_\alpha(\rho_A) \qquad (10)$$

where A and B are two subsystems of the state ρ. Note that Eq. (10) generalizes the definition for $\alpha = 2$ introduced in Ref. [19]. Note that in contrast to the usual mutual informations, $\mathcal{I}_\alpha$ can become negative, however $\mathcal{I}_2$ has still has found interesting applications in the context of many-body phenomena [19, 44, 48].

Using the alternate von-Neumann SRE defined in Eq. (9), we define an alternate version of the mutual von-Neumann SRE as

$$\mathcal{I}_1^{[q]}(\rho) = \tilde{M}_1^{[q]}(\rho) - \tilde{M}_1^{[q]}(\rho_A) - \tilde{M}_1^{[q]}(\rho_B), \qquad (11)$$

which is equivalent to

$$\mathcal{I}_1^{[q]}(|\psi\rangle) = I_2(\rho) - I(q_{\rho_A}, q_{\rho_B}), \qquad (12)$$

where

$$I_2(\rho) = S_2(\rho_A) + S_2(\rho_B) - S_2(\rho) \qquad (13)$$

is the Rényi-2 quantum mutual information and

$$I(q_{\rho_A}, q_{\rho_B}) = H_1(q_{\rho_A}) + H_1(q_{\rho_B}) - H_1(q_\rho) \qquad (14)$$

is the mutual information of the joint probability distribution q_ρ defined in Eq. (6). Note that this relation holds because q_{ρ_A} (q_{ρ_B}) is the marginal probability distribution of q_ρ in A (B). This provides $\mathcal{I}_1^{[q]}(|\psi\rangle)$ with a clear interpretation, as the difference between the quantum mutual information and the classical mutual information of q_ρ defined in subsystems A and B. Importantly, this also leads to a practical advantage in numerical simulations, as we will discuss in Sec. IV A.

We find that $\mathcal{I}_2$, $\mathcal{I}_1$ and $\mathcal{I}_1^{[q]}$ behave similarly, though they can show different signs for the same state. We study them in Appendix B for the TFIM and Heisenberg model.

B. Magic capacity and anti-flatness of the Pauli spectrum

We now introduce the magic capacity in direct analogy to entanglement capacity [62] as

$$C_M(|\psi\rangle) = \text{var}(\hat{M}_1) = \mathop{\mathbb{E}}_{P \sim p(P)}[\ln\left(\langle\psi| P |\psi\rangle^2\right)^2] - M_1^2.$$
(15)

C_M can be thought of as the variance of the estimator $\hat{M}_1$ to compute M_1 via Pauli sampling, and can be computed in $O(N\chi^3\epsilon^{-2})$ time for MPS. Note that, despite of the presence of constant shift in the definition of SRE, the expression for magic capacity is precisely equivalent to that used for entanglement capacity. Interestingly, entanglement capacity is closely related to the anti-flatness of the entanglement spectrum, which has, in turn, been connected to magic [45, 53, 65]. If the explicit form of the SRE is known, the magic capacity can be calculated as [19]

$$C_M = \frac{\mathrm{d}^2\left[(1-\alpha)M_\alpha\right]}{\mathrm{d}\alpha^2}\bigg|_{\alpha=1}.$$
(16)

Similarly to entanglement capacity, the magic capacity is related to the anti-flatness of the Pauli spectrum. Specifically, magic capacity vanishes when the Pauli spectrum is flat, i.e., if the spectrum $p(P) = \text{const}$ for any Pauli string P with non-zero expectation value.

As a toy example, consider a state whose Pauli spectrum is uniform with $\langle\psi| P |\psi\rangle^2 = 1/(2^N + 1)$ for all $P \in \mathcal{P}/\{I\}$. Although this spectrum does not correspond to a physical density matrix, it has been numerically observed to provide a sufficiently good approximation for the Pauli spectrum of a typical state [36]. It is clear that this spectrum is nearly flat, with only the identity operator deviating from a perfectly flat distribution. We can directly compute the SRE and the magic capacity for this uniform state, yielding

$$M_1^{\text{uniform}} = (1 - 2^{-N})\ln\left(2^N + 1\right)$$
(17)

and

$$C_M^{\text{uniform}} = 2^{-N}(1 - 2^{-N})\ln^2(2^N + 1).$$
(18)

In the limit $N \to \infty$, we have $M_1^{\text{uniform}} = N\ln(2)$ and $C_M^{\text{uniform}} \to 0$. The vanishing magic capacity captures the intuition that the Pauli spectrum of the uniform state is asymptotically flat, as expected. We compute the magic capacity of typical states in Appendix C, finding similar scaling with $C_M = \text{const}$, while product states have $C_M \propto N$.

Note that, since the Pauli spectrum always includes the identity operator, $p(I) = 2^{-N}$, it follows that only stabilizer states exhibit flat Pauli spectrum. In other words, magic capacity vanishes if and only if the state is a pure stabilizer state. In fact, magic capacity satisfies similar properties as the SREs: i) For any pure stabilizer state

$|\psi_\text{C}\rangle$, $C_M(|\psi_\text{C}\rangle) = 0$, else $C_M(|\psi\rangle) > 0$. ii) Invariant under Clifford unitaries U_C, i.e. $C_M(U_\text{C}\rho U_\text{C}^\dagger) = C_M(\rho)$, iii) Additive, i.e. $C_M(\rho \otimes \sigma) = C_M(\rho) + C_M(\sigma)$. Thus, we may also view magic capacity as a measure of magic. However, magic capacity captures a different type of complexity, namely the complexity of estimating the magic measure itself. This is different from the conventional notion of a measure of magic, which typically characterizes the hardness of classical simulation by Clifford-based techniques or the number of non-Clifford gates required to prepare the state.

To illustrate this point further, let us consider the estimation of M_α for $\alpha \neq 1$. In this case, the SRE can be estimated by

$$M_\alpha(|\psi\rangle) = \frac{1}{1-\alpha}\ln\mathop{\mathbb{E}}_{P \sim p(P)}[\langle\psi| P |\psi\rangle^{2(\alpha-1)}],$$
(19)

and the variance of this estimator is given by [19]

$$\text{Var}\left(M_\alpha\right) \approx \frac{\exp\left[2(\alpha-1)(M_\alpha - M_{2\alpha-1})\right] - 1}{|\alpha - 1|}.$$
(20)

We see that the variance is dictated by $M_\alpha - M_{2\alpha-1}$. This difference between SREs of different Rényi indices also serves as a measure of the anti-flatness of the Pauli spectrum, analogous to the anti-flatness measures for the entanglement spectrum [53]. This highlights the direct connection between anti-flatness of the Pauli spectrum and the complexity of estimating magic from samples of Pauli operators.

IV. EFFICIENT NUMERICAL METHODS BY PAULI SAMPLING

In this section, we present several algorithms to compute the SREs, mutual von-Neumann SRE, and magic capacity, all of which are based on sampling of Pauli strings.

A. Perfect sampling of mutual von-Neumann SRE for MPS

The von-Neumann SRE $M_1(|\psi\rangle)$ for pure MPS $|\psi\rangle$ can be efficiently computed via perfect sampling as shown in Ref. [17, 18], where the complexity scales as $O(NC_M\chi^3\epsilon^{-2})$, where ϵ is the additive precision. In particular, the error ϵ to estimate M_1 scales as

$$\epsilon \sim \sqrt{C_M/K}$$
(21)

where magic capacity $C_M = \text{var}(\hat{M}_1)$ relates the variance of m_1 over the perfect sampling protocol and is upper bounded by $C_M = O(N^2)$ [18] and K is the number of samples. Notably, C_M can have widely different scaling with N depending on the model and parameter regime.

Similarly, C_M as defined in Eq. (15) can be estimated by via perfect Pauli sampling [17, 18] similarly to M_1.

The mutual von-Neumann SRE $\mathcal{I}_1^{[p]}(|\psi\rangle)$ can be evaluated efficiently using the methods of Ref. [18]. In particular, one has to sample from the normalized Pauli distribution p_ρ as given by Eq. (4), which can be done efficiently as long as ρ has a purification in form of an MPS. The SREs for each of the subsystems A, B, and AB in Eq. (10) can then be evaluated separately in an efficient way. Note that, typically the leading extensive term in the SRE is cancelled out, leaving a subleading term that is much smaller than the SRE. As a result, the estimation of $\mathcal{I}_1^{[p]}(|\psi\rangle)$ is expected to require a significantly larger number of samples compared to the typical estimation of M_1 (see Appendix B).

While a similar approach can be used to compute the alternate version of the mutual von-Neumann SRE $\mathcal{I}_1^{[q]}(|\psi\rangle)$, here we give an even more efficient way to compute $\mathcal{I}_1^{[q]}(|\psi\rangle)$. Using the expression in Eq. (12), we can write

$$\mathcal{I}_1^{[q]}(|\psi\rangle) = S_2(\rho_A) + S_2(\rho_B) - I(q_{\rho_A}, q_{\rho_B}), \qquad (22)$$

where $I(q_{\rho_A}, q_{\rho_B})$ is defined in Eq. (14). The 2-Rényi entanglement entropies can be efficiently computed for MPS via standard methods. Then, $I(q_{\rho_A}, q_{\rho_B})$ can be estimated by

$$I(q_{\rho_A}, q_{\rho_B}) = \mathop{\mathbb{E}}_{P \sim q(P)}[\ln(\mathrm{tr}(\rho P \rho P)) - \ln(\mathrm{tr}(\rho_A P_A \rho_A P_A)) \\ - \ln(\mathrm{tr}(\rho_B P_B \rho_B P_B))]$$

where P_A and P_B are Pauli strings reduced onto subsystem A and B respectively, such that $P = P_A \otimes P_B$. Thus, we need to sample only from one distribution q_ρ, which can be done efficiently for MPS as shown in Ref. [17]. We discuss the technical details in Appendix D. Importantly, the estimation of $\mathcal{I}_1^{[q]}$ is expected to require significantly fewer samples than $\mathcal{I}_1^{[p]}$ because it avoids the need to accurately estimate the individual SREs for the subsystems. We corroborate this computational advantage in the transverse-field Ising model, as shown in Appendix B.

B. Monte Carlo algorithms for mutual 2-SRE

Next, we introduce improved methods to compute the mutual SRE $\mathcal{I}_2$ for $\alpha = 2$. Previous works have estimated $\mathcal{I}_2$ by Monte Carlo sampling of Pauli strings in tensor networks [19, 47, 48, 61]. To do this, one rewrites Eq. (10) as follows:

$$\mathcal{I}_2(\rho) = I_2(\rho) - B(\rho), \qquad (23)$$

where

$$B(\rho) = -\ln\left(\frac{\sum_{P_A \in \mathcal{P}_A} |\mathrm{Tr}(\rho_A P_A)|^4 \sum_{P_B \in \mathcal{P}_B} |\mathrm{Tr}(\rho_B P_B)|^4}{\sum_{P \in \mathcal{P}} |\mathrm{Tr}(\rho P)|^4}\right) \tag{24}$$

and 2-Rényi mutual information $I_2(\rho) = S_2(\rho_A) + S_2(\rho_B) - S_2(\rho)$. In the case of complementary subsystems, the 2-Rényi mutual information is simply given by the 2-Rényi entanglement entropy, which is readily accessible in MPS. To estimate $B(\rho)$, one can sample the Pauli strings according to $\Pi(P) \propto \mathrm{Tr}(\rho P)^4$ and compute

$$B(\rho) = -\ln \mathop{\mathbb{E}}_{P \sim \Pi(P)}\left[\frac{|\mathrm{Tr}(\rho_A P_A)|^4 |\mathrm{Tr}(\rho_B P_B)|^4}{|\mathrm{Tr}(\rho P)|^4}\right], \quad (25)$$

where P is decomposed as $P = P_A \otimes P_B$. Since expectation values of Pauli strings can be efficiently computed in MPS, one can perform Metropolis Monte Carlo scheme by locally updating Pauli string configurations.

The limitation of such an approach is that one must deal with equilibration and autocorrelation times, leading to reduced efficiency. Moreover, the local update scheme need to be tailored to the specific model being studied. In particular, the presence of symmetry may necessitate the design of intricate multi-site update schemes to ensure ergodicity of the Markov chain. While a perfect sampling scheme is able to solve these issues, it cannot be directly applied to estimate $B(\rho)$ since it can only sample from the Pauli distribution $p(P)$.

To mitigate these problems, we propose a method that combines the Monte Carlo and perfect sampling techniques. Specifically, we employ the Metropolis-Hastings Monte Carlo algorithm [66] to sample from $\Pi(P)$. In this scheme, given a current configuration P, a candidate configuration P' is proposed according to some prior distribution $g(P'|P)$, which we assume we can draw from. The candidate is then accepted with probability

$$P_{\mathrm{acc}}(P \to P') = \min\{1, \frac{g(P|P')}{g(P'|P)}\frac{\Pi(P')}{\Pi(P)}\}. \qquad (26)$$

The ideal prior is $g(P'|P) = \Pi(P')$, which is however not available through direct sampling. In Metropolis Monte Carlo, P' is generated by locally updating P and the corresponding $g(P'|P)$ is symmetric in its arguments. Here, we propose different types of prior that approximate the ideal prior $\Pi(P')$, and which can be directly sampled in MPS. These approaches also have the advantage that all samples are independent from each other, and thus can be generated in parallel.

First, we propose to use $p(P')$ as a prior, which is readily available through perfect sampling. Given that $p(P')$ and $\Pi(P')$ correspond to different powers of Pauli strings, we expect that these probability distributions are strongly correlated. This suggests that employing $p(P')$ as the proposal distribution within the Metropolis-Hastings framework could improve sampling efficiency. This intuition is particularly clear for stabilizer states, in which case $p(P)$ and $\Pi(P)$ are identical. More generally, the difference between two probability distributions can be quantified using the Kullback-Leibler divergence, defined as

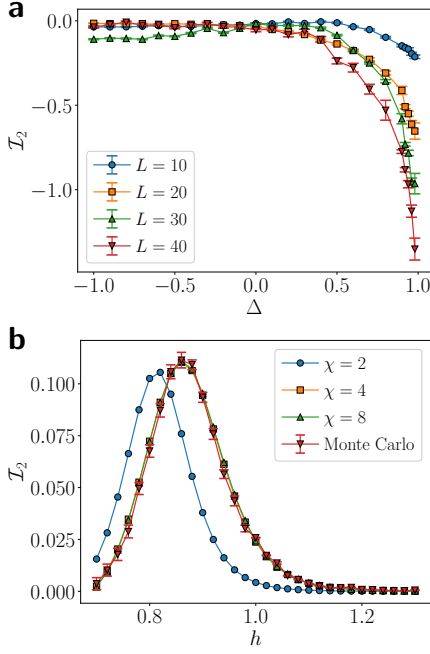$$D_{\mathrm{KL}}(P(x)\|Q(x)) = \sum_x P(x) \ln \frac{P(x)}{Q(x)}, \qquad (27)$$

FIG. 1. Mutual 2-SRE $\mathcal{I}_2$ of the groundstate of the (a) the Heisenberg model with bond dimension $\chi = 20$, and (b) TFIM with $N = 16$. For the TFIM, the Monte Carlo results are obtained with $\chi = 8$ and $\chi' = 2$. The mutual SRE is calculated in respect to two subsystems A, B of size $N/4$ located at the respective boundaries of the chain.

where $P(x)$ and $Q(x)$ are probability distributions. We find that the Kullback-Leibler divergence between $p(P)$ and $\Pi(P)$ is related to the difference of SRE, as follows

$$D_{\mathrm{KL}}(p(P)\|\Pi(P)) = M_1 - M_2. \tag{28}$$

As discussed in Sec. III B, such a difference of SRE characterizes the anti-flatness of Pauli spectrum. This approach thus works best for states with a nearly flat Pauli spectrum. In the case where the spectrum is far from being flat, exponentially many samples may be required for convergence to the desired distribution. We note that a similar exponential sample problem also arises in estimating the 2-SRE through sampling techniques [17, 18]. Nevertheless, the overall cost typically grows much more slowly than that of exact computation [19, 61]. Therefore, even with the potential for high sample complexity in some cases, this approach remains valuable for extending the accessible system sizes.

We briefly illustrate this method for the ground-state of the XXZ or Heisenberg model which is given by

$$H_{\mathrm{XXZ}} = -\sum_{n=1}^{N-1} (\sigma_n^x \sigma_{n+1}^x + \sigma_n^y \sigma_{n+1}^y + \Delta \sigma_n^z \sigma_{n+1}^z) \tag{29}$$

with the anisotropy Δ. The model conserves the total number of excitations. We compute the ground state within the half-filling excitation symmetry sector $N_{\mathrm{p}} = \sum_{n=1}^{N} \sigma_n^z = 0$. In Fig. 1a, we show the mutual 2-SRE $\mathcal{I}_2$

as a function of the field Δ. It has a similar qualitative behavior as the mutual von-Neumann SRE. Further, we observed a significant increase in the statistical errors as the anisotropy approaches $\Delta = 1$. To maintain data quality, we thus required a substantially larger number of samples $K = 10^8$ for $\Delta \geq 0.9$ compared to $K = 10^6$ for $\Delta > 0.9$. This can be seen as a consequence that the anti-flatness of the ground states drastically increases as the anisotropy approaches $\Delta = 1$, as we will demonstrate in Sec. V using the magic capacity C_M.

Another strategy to approximate the probability distribution $\Pi(P)$ is to construct an MPS approximation $|\mathrm{MPS}'\rangle$ of the target MPS by truncating the bond dimension χ to a smaller bond dimension χ'. The distribution $\tilde{\Pi}(P) \propto \langle \mathrm{MPS}'|P|\mathrm{MPS}'\rangle^4$ can be used as an approximation to $\Pi(P)$. For sufficiently small χ', $\tilde{\Pi}(P)$ can be sampled directly by exact contraction of the MPS with a computational cost scaling as $O(\chi'^9)$. This allows us to implement the Metropolis-Hastings scheme by selecting the prior $g(P'|P) = \tilde{\Pi}(P)$. Note that this approach also enables the estimation of mutual magic when the subsystems are separated, a scenario that has found importance in physical phenomena [19, 48, 67]. In Fig. 1b, we compare the mutual SRE obtained by exact contraction with the Monte Carlo estimation for $N = 16$ for the ground state of the TFIM model

$$H_{\mathrm{TFIM}} = -\sum_{k=1}^{N-1} \sigma_k^x \sigma_{k+1}^x - h \sum_{k=1}^{N} \sigma_k^z \tag{30}$$

where we have the field h and choose open boundary conditions. Here, A, B are two subsystems located at the boundary of the chain, each of length $N/4$. For the Monte Carlo estimation, we use $\chi = 8$ and $\chi' = 2$. While the MPS $\chi' = 2$ approximation exhibits deviations from the exact mutual SRE, the samples generated from this approximation can still serve as effective proposals within the Metropolis-Hastings framework. This approach leads to accurate Monte Carlo estimation of the mutual SRE, demonstrating the efficacy of our method.

C. Statevector simulation for Pauli sampling, magic capacity and SRE

Finally, we introduce a statevector simulation method for Pauli sampling, Bell sampling, magic capacity, and von-Neumann SRE with time complexity $O(2^{N/2})$ and memory $O(2^N)$.

Pauli sampling involves sampling from the Pauli distribution $P \sim p_{|\psi\rangle}(P) = 2^{-N} \langle\psi|P|\psi\rangle^2$. It has for example applications in direct estimation of fidelity [68]. Pauli sampling is closely related to Bell sampling $P \sim 2^{-N} \langle\psi^*|P|\psi\rangle^2$, which can be efficiently done in experiment [25, 64, 69–71] with many applications, such as learning stabilizer states [64] with few T-gates [71–73] and estimating magic [24, 25]. In fact, our Pauli sampling algorithm can also be used to perform Bell sampling.
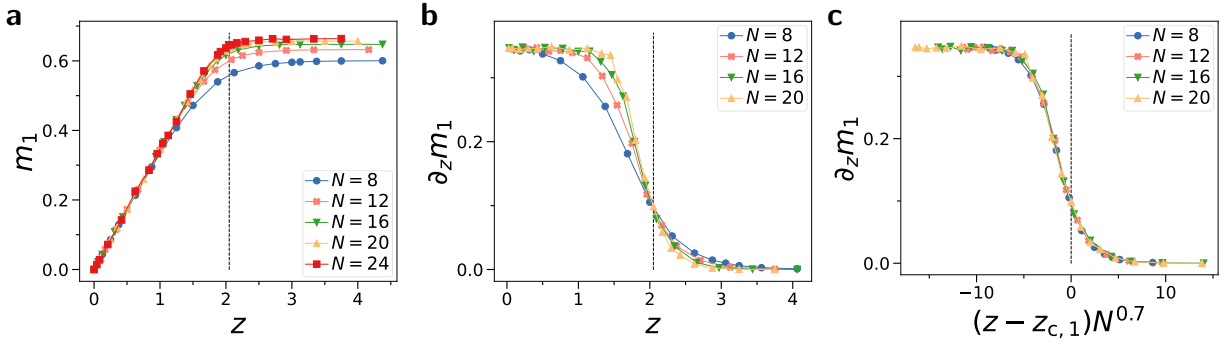
FIG. 2. Von-Neumann SRE density m_1 for Clifford circuits doped with T-gate density $z = N_T/N$. **a)** Average m_1 against z for different qubit numbers N. **b)** $\partial_z m_1$ against z. Curves of $\partial_z m_1$ intersect for all N at saturation transition $z_{c,1}^{fit} \approx 2.05$, which is marked by the dashed black line. **c)** $\partial_z m_1$ against rescaled $(z - z_{c,1}^{fit})N^\gamma$, where we find scaling factor $\gamma \approx 0.7$. After rescaling, the curves collapse for all N, showing the universality of $\partial_z m_1$.
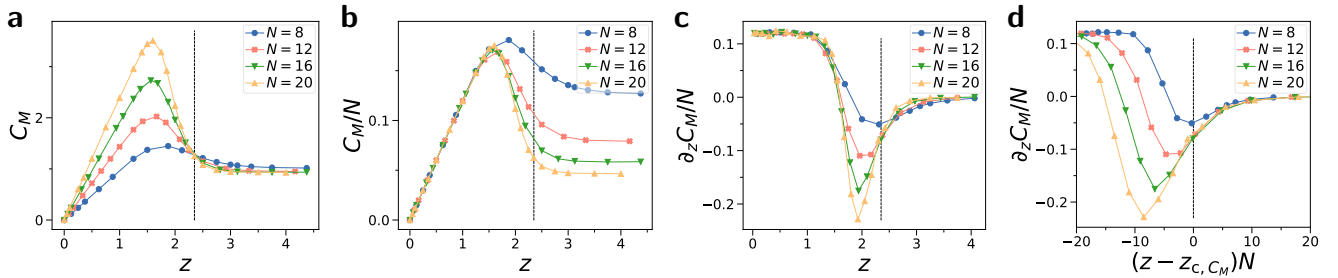
FIG. 3. Magic capacity C_M for Clifford circuits doped with T-gate density $z = N_T/N$. **a)** Magic capacity C_M against z. Curves for all N intersect at a transition point $z_{c,C_M} \approx 2.35$, which is marked by vertical dashed line. We used $K = 10^5$ Pauli samples for $N = 8$ and $N = 12$, while $K = 10^3$ for $N = 16$ and $N = 20$. Data is averaged over at least 100 random instances. **b)** Magic capacity density C_M/N, which is rescaled with $1/N$. **c)** Derivative of magic capacity density $\partial_z C_M/N$ against z. Curves for $N \geq 12$ intersect at transition point $z_{c,C_M} \approx 2.35$. **b)** $\partial_z C_M/N$ against rescaled $(z - z_{c,C_M})N$. Around the transition point z_{c,C_M}, curves for $N \geq 12$ can be made to collapse to a single curve.

From Pauli sampling, one can efficiently compute von-Neumann SREs and magic capacity. Simulating Pauli sampling naively on a classical computer requires storing a 4^N dimensional state in memory, which in general requires too much memory to be practical. To reduce memory load, one could consider Feynmann type simulation algorithms which have lower memory cost, however the trade-off is an excessive computational time [74].

To balance memory and computational time, we provide a hybrid Schrödinger-Feynmann algorithm to sample Pauli P from the distribution $p(P)$, where each sample takes $O(8^{N/2})$ time and $O(2^N)$ memory. The algorithm is presented in detail in Appendix E The main idea of our algorithm is to sample the $2N$ bits of the Pauli in two steps: The first N qubits are sampled with a Feynmann-like algorithm where the state is not explicitly stored in memory. Then, after measuring N qubits the reduced state can be stored fully in memory and the outcomes for the final N qubits are sampled via marginals.

From this, we get an improved method to compute SREs. A naive method to compute SREs is to sum over exponentially many Pauli expectation values $\langle\psi| \sigma |\psi\rangle^{2\alpha}$. This method scales as $O(8^N)$ and has been implemented

for up to 15 qubits. With Pauli sampling, we achieve a square-root speedup to compute the case $\alpha = 1$, allowing us to compute von-Neumann SREs for 24 qubits. Similarly, we can compute the magic capacity via the Pauli sampling.

The detailed algorithm is presented in Appendix F where the code is available on Github from Ref. [75]. Our algorithm gives us an unbiased estimator of $M_1(|\psi\rangle)$, where we can bound the scaling of the estimation error as $\epsilon \sim \sqrt{C_M/K}$, where K is the number of measured samples. We achieve a scaling of a $O(8^{N/2}\epsilon^{-2})$ in time and $O(2^N)$ in memory. Our algorithm has the same asymptotic scaling as the perfect sampling algorithm for MPS with maximal bond dimension $\chi = 2^{N/2}$, but does not need the explicit construction of the MPS, which is convenient for many applications.

V. APPLICATIONS TO MANY-BODY PHENOMENA

We apply the methods in Sec. IV to investigate the mutual von Neumann SRE and magic capacity, both in

the context of ground states and quantum circuits. For the Clifford+T circuits, we perform the statevector simulation in Sec. IV C. For ground states, we obtain them using DMRG, and then employ the MPS Pauli sampling method.

A. Clifford+T circuits

First, we study m_1 and magic capacity C_M to characterize random Clifford circuits doped with T-gates. They are random Clifford circuits U_C interleaved with N_T T-gates $T = \mathrm{diag}(1, \exp(-i\pi/4)$ [25, 76]

$$|\psi(N_T)\rangle = U_C^{(0)}[\prod_{k=1}^{N_T}(T \otimes I_{n-1})U_C^{(k)}]|0\rangle . \qquad (31)$$

Here, we define the T-gate density $z = N_T/N$. It is known that Clifford+T circuits with $z = \mathrm{const}$ become close approximations of Haar random states [34, 76–78], where the exact transition point is not known. Further, it has been observed that Clifford+T circuits saturate the maximal possible value of the SRE M_α in a sharp transition for large N. Such saturation transitions appear at a critical $z_{c,\alpha}$, which depends on the chosen α of the α-SRE [36]. The saturation transition is characterized by a universal behavior of $\partial_z m_\alpha$, where $m_\alpha = M_\alpha/N$ is the magic density and ∂_z is the derivative in respect to z. In particular, one finds that the curves of $\partial_z m_\alpha$ for different N cross at the same $z_{c,\alpha}$. Further, by a proper rescaling, $\partial_z m_\alpha(N)$ can be made to collapse to a single curve for all N [36]. This is hallmark of universal behavior, usually found at phase transitions, where properties of the system become scale-invariant and simple functions of N [79]. The transition points have been found analytically, e.g. $z_{c,0}^{\mathrm{analytical}} = 1$, $z_{c,1}^{\mathrm{analytical}} = 2$ and $z_{c,2}^{\mathrm{analytical}} = \ln(2)/\ln(4/3) \approx 2.409$ [36]. However, the functional shape of the curves $M_\alpha(N)$ around the transition is known analytically only for $\alpha = 2$, while for other α numerical studies for sufficiently large N have been challenging. As Clifford+T circuits are highly entangled quantum states, MPS techniques are not suitable for their simulations. Instead, we use our method for statevector simulation introduced in Sec. IV C to compute M_1 and C_M up to $N = 24$ qubits.

In Fig.2a, we show the von-Neumann SRE density $m_1 = M_1/N$ against T-gate density $z = N_T/N$. We find that it increases linearly with z until it saturates at sufficiently large z. For large N, this transition to maximal m_1 is expected to become sharp, at a characteristic saturation transition point $z_{c,1}$ [36]. In Fig.2b, we plot the derivative $\partial_z m_1$ against z. We find that the curves for all N intersect at $z_{c,1}^{\mathrm{fit}} \approx 2.05$ marked with a dashed black line, which indicates the critical point of the saturation transition. Note that the numeric value matches closely the analytic value of $z_{c,1}^{\mathrm{analytic}} = 2$ derived in Ref. [36] for $\alpha = 1$. Notably, around the critical point, the curves

become universal, i.e. they follow a functional form that has a simple dependence on N. In particular, by rescaling $(z - z_{c,1}^{\mathrm{fit}})N^\gamma$ with $\gamma \approx 0.7$, we find that all curves clearly overlap in Fig.2c.

Next, we study magic capacity C_M in Fig.3, where as we will see observe the transition at a different z_{c,C_M}. In Fig.3a, we show the magic capacity C_M against z. We find that it increases with z, until it peaks and decreases sharply onto a constant, nearly N-independent value. Notably, for large N and z, the value found matches the typical $C_M^{\mathrm{typ}} \approx 0.9348$ for Haar random states derived in Eq. (C3), indicating that at z_{c,C_M} Clifford+T circuits become typical and are good approximations of Haar random states, quantifying predictions of Refs. [34, 76]. Notably, we see that at $z_{c,C_M} \approx 2.35$, curves for different N intersect at a single point which is indicated by the vertical black line. This indicates a transition in C_M at this point, which is notably at a different point than $z_{c,1}$. In Fig.3b, we study the magic capacity density C_M/N. For $z \ll z_{c,C_M}$, we find that $C_M \propto N$, indicating that the capacity increases with N, in contrast to $z > z_{c,C_M}$. Next, in Fig.3c we study the derivative of the magic capacity density $\partial_z C_M/N$. We find that curves for $N \geq 12$ intersect at z_{c,C_M}. We note that small $N = 8$ does not intersect at the saturation transition point due to finite size effects. Further, in Fig.3d, we plot the derivative against rescaled $(z - z_{c,C_M})N$. Here, we find that around z_{c,C_M}, the curves coincide for different N, for $N \geq 12$. This highlights that C_M also undergoes a saturation transition similar to m_α, however the transition happens at larger z.

Finally, we note that the saturation transition in magic capacity z_{c,C_M} implies a transition in the number of samples K needed to estimate M_1. In particular, the error scales as $\epsilon \sim \sqrt{C_M/K}$ as C_M determines the variance of the estimator of M_1 (see Appendix F). In particular, the variance determines the number of sampled Pauli strings needed to estimate M_1 within a given accuracy. Thus, we find that the von-Neumann SRE requires the most samples for $z \approx 1.7$ where C_M shows a peak and scales as $C_M \propto N$. In contrast, for $z > z_{c,C_M}$, C_M is small and independent of N, rendering the estimation of the SRE substantially easier when states become typical.

B. Hamiltonian ground state transitions

Next, we use the magic capacity and mutual magic to characterize transitions in the ground state of Hamiltonians.

First, we study the Heisenberg model as defined in Eq. (29) as function of anisotropy Δ. We show m_1 in Fig. 4a and the mutual SRE in Fig. 4b. Notably, we find that towards $\Delta = 1$, m_1 develops a minima, while $\mathcal{I}_1^{[q]}$ acquires a maximum. Next, we look at the magic capacity C_M (and thus variance of the estimator of M_1) in Fig. 4c,d. We find that crucial information resides in the scaling of C_M with N which we study by plotting
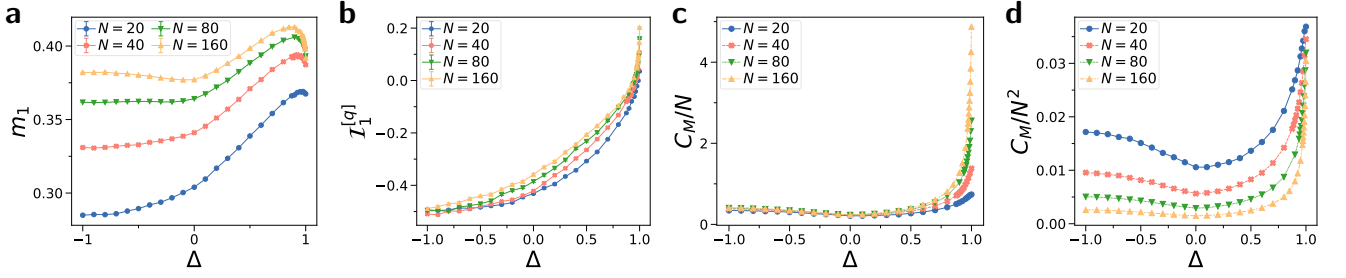
FIG. 4. Von-Neumann SRE for groundstate of Heisenberg model with anisotropy Δ. **a)** $m_1 = M_1/N$, **b)** mutual von-Neumann SRE $\mathcal{I}_1^{[q]}$ for bipartitions of size $N/2$. **c)** Magic capacity density C_M/N against Δ. **d)** Magic capacity C_M rescaled with $1/N^2$. We use $K = 10^5$ samples to estimate m_1 and C_M.

C_M rescaled with powers of N. In Fig. 4c, we find that for $\Delta \ll 1$ we have $C_M \propto N$. In contrast, we find in Fig. 4d $\Delta \approx 1$, the magic capacity scales as $C_M \propto N^2$. Notably, this asymptotically saturates the scaling, as is upper bounded by $C_M = O(N^2)$. Note that this demonstrates the $\Delta = 1$ ground state is a highly atypical state, which shows a quite distinct scaling compared to Haar random states (with $C_M = O(1)$) and product states (with $C_M \propto N$) as shown in Appendix C.

Next, in Fig. 5 we study the ground state of the TFIM and show the von-Neumann SRE density $m_1 = M_1/N$ in Fig. 5a for different N. m_1 peaks close to the critical point $h \approx 1$ and converges to $h = 1$ for increasing N. Similarly, in Fig. 5b, we study the magic capacity C_M. We find that $C_M \propto N$ for all h, and exhibits a minimum at the critical point $h = 1$, indicating that the magic capacity is also sensitive to criticality. Then, we show the mutual von-Neumann SRE $\mathcal{I}_1^{[q]}$ in Fig. 5c and 2-SRE $\mathcal{I}_2$ in Fig. 5d. We find that both shows a sharp peak at the critical point $h = 1$. Notably, both $\mathcal{I}_2$ and $\mathcal{I}_1^{[q]}$ do not increase substantially with N at the critical point, highlighting that there is no logarithmic divergence and only constant corrections with N. We can use the minima of C_M and $\mathcal{I}_2$, as well as the peaks of m_1 and $\mathcal{I}_1^{[q]}$ to determine the critical field of the TFIM. We adopt the fitting procedure of Ref. [16], which used m_2. Here, we track the field $h_0(N)$ with extremal value of m_1, C_M, $\mathcal{I}_2$ and $\mathcal{I}_1^{[q]}$ for different N, and then extrapolate the fit to $N \to \infty$ to determine $h_c^{\text{fit}} \equiv h_0(N \to \infty)$. We demonstrate this procedure in Appendix G, where we find accurate match between true critical field $h_c = 1$ and our fits h_c^{fit}.

The mutual SRE is also highly useful to determine the critical point of the TFIM independent of the chosen local basis. The amount of magic changes when the local basis of the Hamiltonian is rotated as $H' = V^{\otimes N} H V^{\otimes N\dagger}$ with single-qubit unitary V. As a result, depending on V, there may be no extremum in M_α at the critical point [16]. In contrast, we find that mutual SREs such as $\mathcal{I}_1^{[q]}$ or $\mathcal{I}_2$ show a peak at $h = 1$ independent of the choice of V. We perform a scaling analysis for $\mathcal{I}_2$ in Appendix H, where we find via fitting a critical point $h_c^{\text{fit}} \approx 1.004$. We highlight this for the choice $V_y = \exp(-i\sigma^y \pi/8)$ in Fig. 6.

While in Fig. 6a m_2 does not show an extremum at the critical point (the observed minimum does not converge towards $h = 1$ even for large N [16]), a minimum at $h = 1$ clearly emerges for $\mathcal{I}_2$ in Fig. 6b. We study the criticality via mutual SRE further in Appendix H for different basis and types of mutual SRE.

Finally, we note that recent conformal field theory (CFT) calculations [60] reveal that the term $B(\rho)$ in Eq. (23) displays a universal logarithmic scaling. In Ising CFT, the logarithmic scaling has the same prefactor as the 2-Rényi mutual information I_2. As a result, the logarithmic scaling term cancels out in the mutual 2-SRE, leaving a constant term that is likely non-universal. Our data is consistent with the CFT prediction, as we find no logarithmic divergence in the standard basis (i.e. Fig. 5). Nevertheless, the mutual SRE still displays non-analytic behavior at the critical point in this case.

VI. DISCUSSION

In this work, we present several advancements in the efficient estimation and characterization of magic in many-body quantum systems and quantum circuits.

First, we introduced the mutual von Neumann SRE as a proxy of nonlocal magic, which can be efficiently computed using perfect Pauli sampling in $O(N\chi^3)$ time for MPS. We find two different variants $\mathcal{I}_1$ and $\mathcal{I}_1^{[q]}$, where for the latter we provide a simpler algorithm for computation. Moreover, we develop two new algorithms based on Metropolis-Hastings Monte Carlo methods to compute the mutual 2-SRE. Remarkably, our analysis reveals that mutual SREs consistently identify critical points in the TFIM regardless of the local basis chosen. This contrasts sharply with the limitations of the bare SRE, which fails to detect criticality under basis rotations [16]. This demonstrates the enhanced robustness of mutual SREs for characterizing quantum phase transitions, independent of the local basis.

Curiously, we find that the mutual SRE does not exhibit logarithmic divergence at the critical point in the natural basis, which is also in agreement with the CFT prediction [60]. This behavior is in contrast to the find-
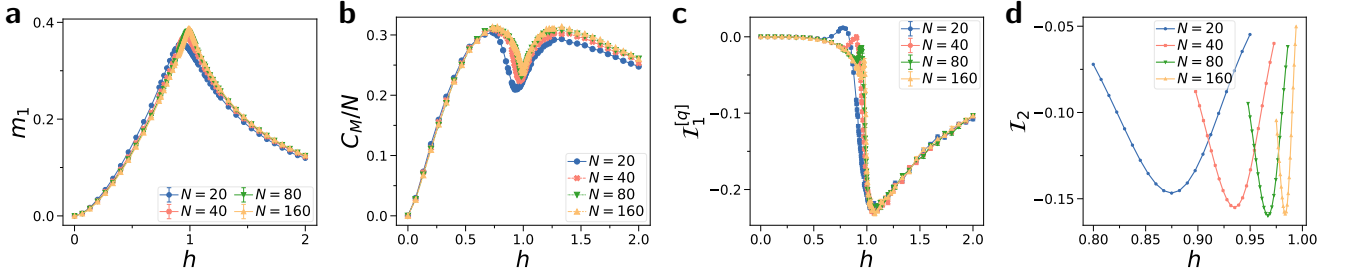
FIG. 5. Von-Neumann SRE for groundstate of TFIM against field h, where we choose the Hamiltonian in the standard computational basis. **a)** $m_1 = M_1/N$ and **b)** C_M rescaled by $1/N$. **c)** Mutual von-Neumann SRE $\mathcal{I}_1^{[q]}$ and **d)** Mutual 2-SRE for bipartitions of size $N/2$. We use $K = 10^5$ Pauli samples to estimate m_1, C_M and $\mathcal{I}_1^{[q]}$.
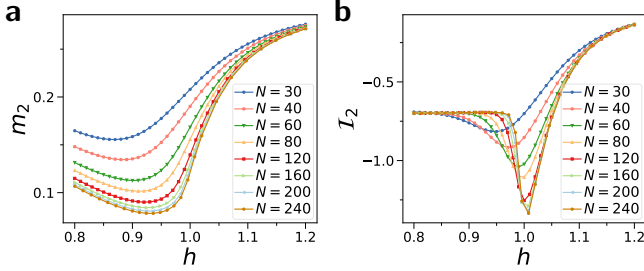

FIG. 6. 2-SRE for groundstate of TFIM with field h in a locally rotated basis $V_y = \exp(-i\sigma^y \pi/8)$ for different N to determine critical point $h = 1$. We show **a)** m_2 and **b)** $\mathcal{I}_2$.

ings of previous works [44, 61], which found logarithmic scaling of mutual magic in critical ground states [61] and monitored circuits [44]. This difference is possibly due to the fact that the latter two works employed genuine measures of magic for mixed states to define the mutual magic. This calls into question about the role of mutual SRE as a proxy of nonlocal magic. The efficient methods to compute mutual SRE we developed in this work would enable systematic investigation of the mutual SRE, paving the way for a deeper understanding on its relation to nonlocal magic.

Further, we define the magic capacity C_M, in analogy to entanglement capacity, and discuss its connection to the anti-flatness of the Pauli spectrum. This parallels the relationship between entanglement capacity and the anti-flatness of the entanglement spectrum. We show that magic capacity can be viewed as a measure of magic, which however probes a different type of complexity. Namely, it characterizes the sampling complexity to compute the von-Neumann SRE. Importantly, magic capacity can also be efficiently computed for MPS in $O(N\chi^3)$ time.

Using C_M, we can characterize the T-gate density z that is necessary to generate typical states using Clifford+T circuits. We find that the curves of C_M and $\partial_z C_M/N$ for different N intersect at a single point at $z_{c,C_M} \approx 2.35$, indicating a saturation transition at z_{c,C_M}. The transition is accompanied by a shift in the scal-

ing of C_M, from volume-law to being independent of N. This saturation transition also places a lower bound of $z \gtrsim 2.35$ needed for Clifford+T circuits to approximate Haar random states [34, 76, 77]. This contrasts 8-point OTOCs or M_1, which are less accurate indicators of Haar randomness, as they saturate already for smaller $z \gtrsim 2$ [77]. The saturation transition in C_M also implies a sharp change in the number of Pauli samples K needed to estimate M_1: The estimation of M_1 requires only a number of samples which is independent of N whenever $z \gtrsim z_{c,C_M}$.

In fact, we find that the magic capacity beyond the transition point is consistent with that of typical states. In Ref. [80], a quantity called filtered SRE was introduced to distinguish the magic of typical and atypical states. It was shown that the density of the filtered SRE, as a function of the Rényi index α, exhibits distinct behavior for these two classes of states. The filtered SRE was specifically designed to address the problem that this distinguishing feature is exponentially suppressed in the standard SRE. Our work establishes that this distinction can also be observed in the magic capacity, offering an alternative method for distinguishing typical and atypical states, which we corroborate through our numerical results. Because the distinguishing feature lies in the *scaling* of magic capacity, rather than simply the density as in the filtered SRE, this new method offers a more pronounced separation between typical and atypical states. Furthermore, it has a particular advantage of efficient computability via Pauli sampling.

Finally, we investigate the magic capacity in the ground state of the Heisenberg and TFIM. For the Heisenberg model, we find that for $\Delta \ll 1$, the magic capacity scales linearly with system size, $C_M \propto N$. However, at $\Delta \approx 1$, the scaling transitions to $C_M \propto N^2$, which asymptotically saturates the known upper bound $C_M = O(N^2)$. For the Ising model, we find that the capacity scales as $C_M \propto N$ for all h, but exhibits a characteristic dip at the critical point $h = 1$. This highlights that the magic capacity can be used to characterize the ground states of Hamiltonians.

Our work opens several avenues for future research. First, magic capacity could be applied as an efficient

tool to characterize transitions of magic in random quantum circuits, driven by competition of Clifford and non-Clifford resources [42–44, 81]. Furthermore, it is instructive to connect the mutual α-SRE to the notion of long-range magic as magic that cannot be removed by finite-depth circuits [57]. Finally, it would be worth exploring other aspects of magic that may offer enhanced robustness in detecting quantum correlations, criticality, and other crucial physical phenomena, such as topological order or gauge theory. This could uncover novel connections between magic and fundamental quantum properties.

ACKNOWLEDGMENTS

[1] S. Bravyi and A. Kitaev, Universal quantum computation with ideal clifford gates and noisy ancillas, Phys. Rev. A **71**, 022316 (2005).

[2] V. Veitch, S. H. Mousavian, D. Gottesman, and J. Emerson, The resource theory of stabilizer quantum computation, New J. Phys. **16**, 013009 (2014).

[3] D. Gottesman, *Stabilizer codes and quantum error correction. Caltech Ph. D*, Ph.D. thesis, Thesis, eprint: quant-ph/9705052 (1997).

[4] M. A. Nielsen and I. L. Chuang, *Quantum Computation and Quantum Information: 10th Anniversary Edition* (Cambridge University Press, 2011).

[5] A. Y. Kitaev, Fault-tolerant quantum computation by anyons, Ann. Phys. **303**, 2 (2003).

[6] B. Eastin and E. Knill, Restrictions on transversal encoded quantum gate sets, Phys. Rev. Lett. **102**, 110502 (2009).

[7] D. Gottesman, Theory of fault-tolerant quantum computation, Phys. Rev. A **57**, 127 (1998).

[8] D. Gottesman, The heisenberg representation of quantum computers, arXiv quant-ph/9807006 (1998).

[9] S. Aaronson and D. Gottesman, Improved simulation of stabilizer circuits, Phys. Rev. A **70**, 052328 (2004).

[10] E. Chitambar and G. Gour, Quantum resource theories, Rev. Mod. Phys. **91**, 025001 (2019).

[11] S. Bravyi, D. Browne, P. Calpin, E. Campbell, D. Gosset, and M. Howard, Simulation of quantum circuits by low-rank stabilizer decompositions, Quantum **3**, 181 (2019).

[12] Z.-W. Liu and A. Winter, Many-body quantum magic, PRX Quantum **3**, 020333 (2022).

[13] M. Howard and E. Campbell, Application of a resource theory for magic states to fault-tolerant quantum computing, Phys. Rev. Lett. **118**, 090501 (2017).

[14] P. S. Tarabunga, M. Frau, T. Haug, E. Tirrito, and L. Piroli, A nonstabilizerness monotone from stabilizerness asymmetry, arXiv:2411.05766 (2024).

[15] L. Leone, S. F. E. Oliviero, and A. Hamma, Stabilizer rényi entropy, Phys. Rev. Lett. **128**, 050402 (2022).

[16] T. Haug and L. Piroli, Quantifying nonstabilizerness of matrix product states, Phys. Rev. B **107**, 035148 (2023).

[17] T. Haug and L. Piroli, Stabilizer entropies and nonstabilizerness monotones, Quantum **7**, 1092 (2023).

[18] G. Lami and M. Collura, Nonstabilizerness via perfect pauli sampling of matrix product states, Phys. Rev. Lett. **131**, 180401 (2023).

[19] P. S. Tarabunga, E. Tirrito, T. Chanda, and M. Dalmonte, Many-body magic via pauli-markov chains—from criticality to gauge theories, PRX Quantum **4**, 040317 (2023).

[20] P. S. Tarabunga, E. Tirrito, M. C. Bañuls, and M. Dalmonte, Nonstabilizerness via matrix product states in the pauli basis, Phys. Rev. Lett. **133**, 010601 (2024).

[21] P. S. Tarabunga and C. Castelnovo, Magic in generalized rokhsar-kivelson wavefunctions, Quantum **8**, 1347 (2024).

[22] Z. Liu and B. K. Clark, Nonequilibrium quantum monte carlo algorithm for stabilizer rényi entropy in spin systems, Physical Review B **111**, 10.1103/physrevb.111.085144 (2025).

[23] Y.-M. Ding, Z. Wang, and Z. Yan, Evaluating many-body stabilizer rényi entropy by sampling reduced pauli strings: singularities, volume law, and nonlocal magic, arxiv:2501.12146 (2025).

[24] T. Haug and M. Kim, Scalable measures of magic resource for quantum computers, PRX Quantum **4**, 010301 (2023).

[25] T. Haug, S. Lee, and M. S. Kim, Efficient quantum algorithms for stabilizer entropies, Phys. Rev. Lett. **132**, 240602 (2024).

[26] S. F. E. Oliviero, L. Leone, A. Hamma, and S. Lloyd, Measuring magic on a quantum processor, npj Quantum Information **8**, 148 (2022).

[27] D. Bluvstein, S. J. Evered, A. A. Geim, S. H. Li, H. Zhou, T. Manovitz, S. Ebadi, M. Cain, M. Kalinowski, D. Hangleiter, *et al.*, Logical quantum processor based on reconfigurable atom arrays, Nature **626**, 58 (2024).

[28] T. Haug and P. S. Tarabunga, Efficient witnessing and testing of magic in mixed quantum states, arxiv:2504.18098 (2025).

[29] S. F. E. Oliviero, L. Leone, and A. Hamma, Magic-state resource theory for the ground state of the transverse-field ising model, Phys. Rev. A **106**, 042426 (2022).

[30] P. R. N. Falcão, P. S. Tarabunga, M. Frau, E. Tirrito, J. Zakrzewski, and M. Dalmonte, Nonstabilizerness in u(1) lattice gauge theory, Physical Review B **111**, 10.1103/physrevb.111.l081102 (2025).

[31] A. Sinibaldi, A. F. Mello, M. Collura, and G. Carleo, Non-stabilizerness of neural quantum states, arXiv:2502.09725 (2025).

[32] H. Timsina, Y.-M. Ding, E. Tirrito, P. S. Tarabunga, B.-B. Mao, M. Collura, Z. Yan, and M. Dalmonte, Robustness of magic in the quantum ising chain via quantum monte carlo tomography, arxiv:2507.12902 (2025).

[33] G. Lami, T. Haug, and J. De Nardis, Quantum state designs with clifford-enhanced matrix product states, PRX Quantum **6**, 10.1103/prxquantum.6.010345 (2025).

[34] L. Leone, S. F. E. Oliviero, Y. Zhou, and A. Hamma, Quantum chaos is quantum, Quantum **5**, 453 (2021).

[35] R. J. Garcia, K. Bu, and A. Jaffe, Resource theory of quantum scrambling, Proceedings of the National Academy of Sciences **120**, e2217031120 (2023).

[36] T. Haug, L. Aolita, and M. Kim, Probing quantum complexity via universal saturation of stabilizer entropies, Quantum **9**, 1801 (2025).

[37] X. Turkeshi, E. Tirrito, and P. Sierant, Magic spreading in random quantum circuits, Nature Communications **16**, 10.1038/s41467-025-57704-x (2025).

[38] E. Tirrito, X. Turkeshi, and P. Sierant, Anticoncentration and magic spreading under ergodic quantum dynamics, arxiv:2412.10229 (2024).

[39] P. R. N. Falcão, P. Sierant, J. Zakrzewski, and E. Tirrito, Magic dynamics in many-body localized systems, arxiv:2503.07468 (2025).

[40] N. Dowling, P. Kos, and X. Turkeshi, Magic of the heisenberg picture, arxiv:2408.16047 (2025).

[41] E. Tirrito, P. S. Tarabunga, D. S. Bhakuni, M. Dalmonte, P. Sierant, and X. Turkeshi, Universal spreading of nonstabilizerness and quantum transport, arxiv:2506.12133 (2025).

[42] G. E. Fux, E. Tirrito, M. Dalmonte, and R. Fazio, Entanglement – nonstabilizerness separation in hybrid quantum circuits, Phys. Rev. Res. **6**, L042030 (2024).

[43] M. Bejan, C. McLauchlan, and B. Béri, Dynamical magic transitions in monitored clifford+ t circuits, PRX Quantum **5**, 030332 (2024).

[44] P. S. Tarabunga and E. Tirrito, Magic transition in measurement-only circuits, arXiv:2407.15939 (2024).

[45] E. Tirrito, P. S. Tarabunga, G. Lami, T. Chanda, L. Leone, S. F. Oliviero, M. Dalmonte, M. Collura, and A. Hamma, Quantifying nonstabilizerness through entanglement spectrum flatness, Physical Review A **109**, L040401 (2024).

[46] A. Gu, S. F. Oliviero, and L. Leone, Magic-induced computational separation in entanglement theory, arXiv preprint arXiv:2403.19610 (2024).

[47] M. Frau, P. Tarabunga, M. Collura, M. Dalmonte, and E. Tirrito, Nonstabilizerness versus entanglement in matrix product states, Physical Review B **110**, 045101 (2024).

[48] M. Frau, P. S. Tarabunga, M. Collura, E. Tirrito, and M. Dalmonte, Stabilizer disentangling of conformal field theories, SciPost Physics **18**, 10.21468/scipostphys.18.5.165 (2025).

[49] N. Dowling, K. Modi, and G. A. L. White, Bridging entanglement and magic resources through operator space, arxiv:2501.18679 (2025).

[50] X. Turkeshi, M. Schirò, and P. Sierant, Measuring nonstabilizerness via multifractal flatness, Physical Review A **108**, 042408 (2023).

[51] J. Huang, X. Qian, and M. Qin, Non-stabilizerness entanglement entropy: a measure of hardness in the classical simulation of quantum many-body systems, arXiv preprint arXiv:2409.16895 (2024).

[52] D. Qian and J. Wang, Quantum non-local magic, arXiv:2502.06393 (2025).

[53] C. Cao, G. Cheng, A. Hamma, L. Leone, W. Munizzi, and S. F. E. Oliviero, Gravitational back-reaction is magical, arXiv:2403.07056 (2024).

[54] C. D. White, C. Cao, and B. Swingle, Conformal field theories are magical, Phys. Rev. B **103**, 075145 (2021).

[55] S. Sarkar, C. Mukhopadhyay, and A. Bayat, Characterization of an operational quantum resource in a critical many-body system, New J. Phys. **22**, 083077 (2020).

[56] J. R. Fliss, Knots, links, and long-range magic, Journal of High Energy Physics **2021**, 10.1007/jhep04(2021)090 (2021).

[57] D. A. Korbany, M. J. Gullans, and L. Piroli, Long-range nonstabilizerness and phases of matter, arxiv:2502.19504 (2025).

[58] F. Wei and Z.-W. Liu, Long-range nonstabilizerness from topology and correlation, arxiv:2503.04566 (2025).

[59] J. A. Montañà López and P. Kos, Exact solution of long-range stabilizer rényi entropy in the dual-unitary xxz model*, Journal of Physics A: Mathematical and Theoretical **57**, 475301 (2024).

[60] M. Hoshino, M. Oshikawa, and Y. Ashida, Stabilizer rényi entropy and conformal field theory, arxiv:2503.13599 (2025).

[61] P. S. Tarabunga, Critical behaviors of non-stabilizerness in quantum spin chains, Quantum **8**, 1413 (2024).

[62] J. de Boer, J. Järvelä, and E. Keski-Vakkuri, Aspects of capacity of entanglement, Physical Review D **99**, 10.1103/physrevd.99.066012 (2019).

[63] L. Leone and L. Bittel, Stabilizer entropies are monotones for magic-state resource theory, Physical Review A **110**, L040403 (2024).

[64] A. Montanaro, Learning stabilizer states by bell sampling, arXiv:1707.04012 (2017).

[65] M. Viscardi, M. Dalmonte, A. Hamma, and E. Tirrito, Interplay of entanglement structures and stabilizer entropy in spin models, arxiv:2503.08620 (2025).

[66] W. K. Hastings, Monte carlo sampling methods using markov chains and their applications, Biometrika **57**, 97–109 (1970).

[67] J. A. Montañà López and P. Kos, Exact solution of long-range stabilizer rényi entropy in the dual-unitary xxz model*, Journal of Physics A: Mathematical and Theoretical **57**, 475301 (2024).

[68] S. T. Flammia and Y.-K. Liu, Direct fidelity estimation from few pauli measurements, Physical review letters **106**, 230501 (2011).

[69] D. Gross, S. Nezami, and M. Walter, Schur–weyl duality for the clifford group with applications: Property testing, a robust hudson theorem, and de finetti representations, Communications in Mathematical Physics **385**, 1325 (2021).

[70] C.-Y. Lai and H.-C. Cheng, Learning quantum circuits of some t gates, IEEE Transactions on Information Theory **68**, 3951 (2022).

[71] D. Hangleiter and M. J. Gullans, Bell sampling from quantum circuits, Physical Review Letters **133**, 020601 (2024).

[72] S. Grewal, V. Iyer, W. Kretschmer, and D. Liang, Efficient learning of quantum states prepared with few non-clifford gates, arXiv:2305.13409 (2023).

[73] L. Leone, S. F. Oliviero, and A. Hamma, Learning t-doped stabilizer states, Quantum **8**, 1361 (2024).

[74] S. Aaronson and L. Chen, Complexity-theoretic foundations of quantum supremacy experiments, arXiv:1612.05903 (2016).

[75] T. Haug, Code for pauli sampling, magic capac-

ity and von neumann stabilizer rényi entropy of arbitrary states, https://github.com/txhaug/neumann_stabilizer_entropy.

[76] J. Haferkamp, F. Montealegre-Mora, M. Heinrich, J. Eisert, D. Gross, and I. Roth, Efficient unitary designs with a system-size independent number of non-clifford gates, Communications in Mathematical Physics , 1 (2022).

[77] L. Leone, S. F. Oliviero, S. Lloyd, and A. Hamma, Learning efficient decoders for quasichaotic quantum scramblers, Physical Review A **109**, 022429 (2024).

[78] B. Magni, A. Christopoulos, A. De Luca, and X. Turkeshi, Anticoncentration in clifford circuits and beyond: From random tensor networks to pseudo-magic states, arXiv preprint arXiv:2502.20455 (2025).

[79] A. Osterloh, L. Amico, G. Falci, and R. Fazio, Scaling of entanglement close to a quantum phase transition, Nature **416**, 608 (2002).

[80] X. Turkeshi, A. Dymarsky, and P. Sierant, Pauli spectrum and nonstabilizerness of typical quantum many-body states, Physical Review B **111**, 10.1103/physrevb.111.054301 (2025).

[81] P. Niroula, C. D. White, Q. Wang, S. Johri, D. Zhu, C. Monroe, C. Noel, and M. J. Gullans, Phase transition in magic with random quantum circuits, Nature Physics **20**, 1786–1792 (2024).

[82] M. Fishman, S. White, and E. Stoudenmire, The itensor software library for tensor network calculations, SciPost Physics Codebases , 004 (2022).

[83] M. Hinsche, M. Ioannou, S. Jerbi, L. Leone, J. Eisert, and J. Carrasco, Efficient distributed inner product estimation via pauli sampling, arXiv:2405.06544 (2024).

Appendix

We provide proofs and additional details supporting the claims in the main text.

Appendix A: Proof of marginals for probability distribution $q_\rho(P)$

In the main text, we consider the alternative probability distribution over Pauli strings P as

$$q_\rho(P) = 2^{-N}\text{tr}(\rho P \rho P). \tag{A1}$$

A nice property of q_ρ is that, for any subsystem A and its complement A^c, the distribution for the reduced density matrix $\rho_A = \text{tr}_{A^c}(\rho)$ is simply the marginal distribution of q_ρ in A. In other words,

$$q_{\rho_A}(P_A) = \sum_{P \in \mathcal{P}_{A^c}} q_\rho(P_A \otimes P) \tag{A2}$$

for any $P_A \in \mathcal{P}_A$.

This can be shown as follows. First, we rewrite

$$\sum_{P \in \mathcal{P}_{A^c}} q_\rho(P_A \otimes P) = 2^{-N}\text{tr}\left(P_A \otimes I_{A^c} \rho P_A \otimes I_{A^c} \sum_{P \in \mathcal{P}_{A^c}} I_A \otimes P \rho I_A \otimes P\right). \tag{A3}$$

Now, we can see that $\sum_{P \in \mathcal{P}_{A^c}} I_A \otimes P \rho I_A \otimes P$ is a Pauli twirl over partition A^c, which is a 1-design and thus leaves only the identity invariant. In particular, one can repeatedly use the identity $\sum_{P \in \mathcal{P}_1} P(.)P = 2I_1\text{tr}_1(.)$ [17] to show that

$$\sum_{P \in \mathcal{P}_{A^c}} I_A \otimes P \rho I_A \otimes P = 2^{N_{A^c}} \rho_A \otimes I_{A^c}. \tag{A4}$$

Using this result, we get

$$\sum_{P \in \mathcal{P}_{A^c}} q_\rho(P_A \otimes P) = 2^{-N_A}\text{tr}(P_A \otimes I_{A^c} \rho P_A \otimes I_{A^c} \rho_A \otimes I_{A^c}) \tag{A5}$$

$$= 2^{-N_A}\text{tr}(\text{tr}_{A^c}(P_A \otimes I_{A^c} \rho P_A \otimes I_{A^c} \rho_A \otimes I_{A^c}) = 2^{-N_A}\text{tr}(P_A \rho_A P_A \rho_A)) \tag{A6}$$

$$\equiv q_{\rho_A}(P_A). \tag{A7}$$

Appendix B: Comparison of mutual SREs

In this section, we compare the different types of mutual SREs as introduced in the main text. We study the mutual 2-SRE $\mathcal{I}_2$, mutual von-Neumann SRE $\mathcal{I}_1^{[p]}$ via $\mathrm{tr}(\rho P)^2$, an $\mathcal{I}_1^{[q]}$ via $\mathrm{tr}(\rho P \rho P)$.

First, we study the ground state of the TFIM in Fig. S1a where we choose a low number of qubits $N = 12$ and large number of qubits $N = 80$ in Fig. S1b. For $N = 80$, we estimate $\mathcal{I}_1^{[p]}$ using $K = 2 \times 10^6$ Pauli samples, while for $\mathcal{I}_1^{[q]}$ we use much lower $K = 10^5$ samples. We note that $\mathcal{I}_1^{[p]}$ requires significantly more samples to estimate due the p distribution of a subsystem not being a marginal for the full distribution, thus increasing the variance of the estimator.

Next, we study the Heisenberg model in Fig. S2. We find find that $\mathcal{I}_2$ decreases towards $\Delta = 1$, while $\mathcal{I}_1^{[q]}$ and $\mathcal{I}_1^{[p]}$ increase. Notably, we find that for large N and $\Delta \approx 1$, $\mathcal{I}_1^{[q]}$ and $\mathcal{I}_1^{[p]}$ show different scalings: $\mathcal{I}_1^{[q]}$ is constant, while $\mathcal{I}_1^{[p]}$ scales with N.
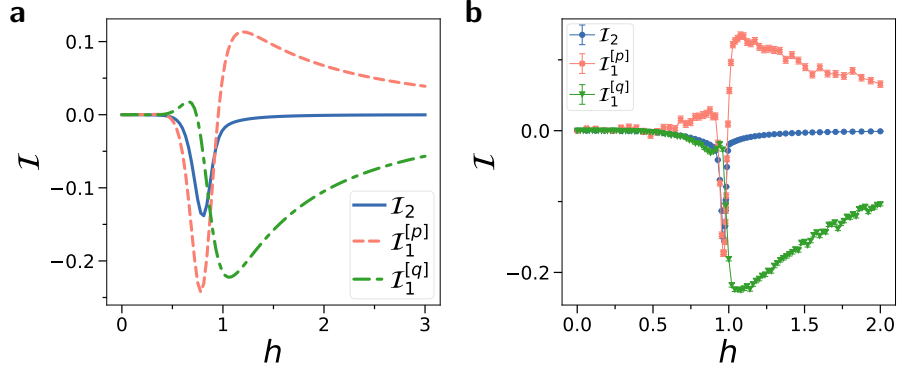

FIG. S1. Comparison of mutual 2-SRE $\mathcal{I}_2$, mutual von-Neumann SRE $\mathcal{I}_1^{[p]}$ via $\mathrm{tr}(\rho P)^2$, and $\mathcal{I}_1^{[q]}$ via $\mathrm{tr}(\rho P \rho P)$. We show bipartition at the center of the chain with **a)** $N = 12$ and **b)** $N = 80$ qubits in total.
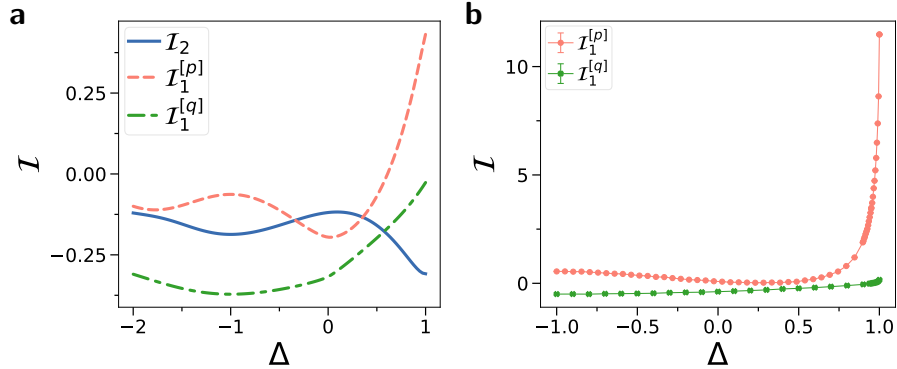

FIG. S2. Different types of mutual magic for ground state of Heisenberg model for anisotropy Δ. Comparison of mutual 2-SRE $\mathcal{I}_2$, mutual von-Neumann SRE $\mathcal{I}_1^{[q]}$ via $\mathrm{tr}(\rho P \rho P)$, and its formulation $\mathcal{I}_1^{[p]}$ via $\mathrm{tr}(\rho P)^2$. We show bipartition at the center of the chain with **a)** $N = 12$ and **b)** $N = 80$ qubits in total.

Now, we study the scaling of mutual magic $\mathcal{I}$ in more detail. While mutual magic is usually independent of N, we find classes of states where it scales with N. In particular, we study a magical GHZ state

$$|\psi_{\mathrm{mGHZ}}\rangle = \frac{1}{\sqrt{2}} \exp(-i\pi/8\sigma^z)^{\otimes N} \exp(-i\beta/2\sigma^y)^{\otimes N} (|00\ldots0\rangle + |11\ldots1\rangle) \tag{B1}$$

where each qubit is rotated by $\exp(-i\pi/8\sigma^z) \exp(-i\beta/2\sigma^y)$ with $\beta = \arccos(1/\sqrt{3})$, which corresponds to the single-qubit rotation that induces the most magic. For $\mathcal{I}_1^{[q]}(|\psi_{\mathrm{mGHZ}}\rangle)$ and $\mathcal{I}_2(|\psi_{\mathrm{mGHZ}}\rangle)$, the mutual magic is positive and constant with N. In contrast, we observe $\mathcal{I}_1^{[p]}(|\psi_{\mathrm{mGHZ}}\rangle) \propto -N$. We believe this may originate from the fact that the

p distribution on subsystems is not a marginal distribution with respect to the full system. This finding indicates that the mutual magic based on p distribution may not be related to the notion of long-range magic as magic that cannot be removed by finite-depth circuits [57, 58], and future work may focus on q distribution to establish a connection.
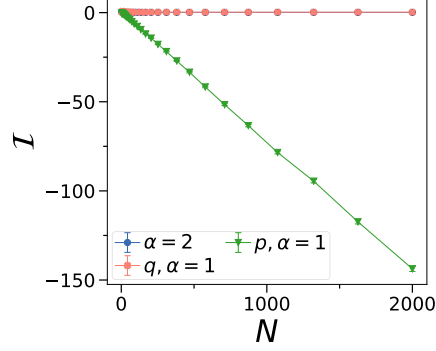

FIG. S3. Different types of mutual magic for a magical GHZ state as defined in Eq. (B1). Comparison of mutual 2-SRE $\mathcal{I}_2$, mutual von-Neumann SRE $\mathcal{I}_1^{[q]}$ via $\mathrm{tr}(\rho P \rho P)$, and its formulation $\mathcal{I}_1^{[p]}$ via $\mathrm{tr}(\rho P)^2$. We show bipartition at the center of the chain with $N = 80$ qubits in total.

Appendix C: Magic capacity of typical states

The phenomenological SRE of typical states was derived in Ref. [80], which reads for large N

$$M_\alpha^{\mathrm{typ}} = \frac{1}{1-\alpha} \ln \left[\frac{(\eta-1)(2b)^\alpha \Gamma\left(\alpha + \frac{1}{2}\right)}{\sqrt{\pi} d} + \frac{1}{d} \right], \tag{C1}$$

where $\Gamma(x)$ is the gamma function, $b = (d/2 + 1)^{-1}$, $d = 2^N$, and $\eta = d^2$ ($\eta = d(d+1)/2$) for complex (real) typical states. In the limit of large N, the average von-Neumann SRE is given by

$$M_1^{\mathrm{typ}} = \lim_{\alpha \to 1} M_\alpha^{\mathrm{typ}} = N \ln(2) - 2 \ln(2) - \frac{\Gamma'(3/2)}{\Gamma(3/2)}, \tag{C2}$$

and the magic capacity, computed using Eq. (16), is given by

$$C_M^{\mathrm{typ}} = \frac{\Gamma''(3/2)}{\Gamma(3/2)} - \left(\frac{\Gamma'(3/2)}{\Gamma(3/2)} \right)^2 \approx 0.934802\ldots. \tag{C3}$$

We see that the magic capacity becomes constant in the limit $N \to \infty$.

This behavior can be contrasted with the magic capacity of the (atypical) tensor product of single-qubit state $|\Theta\rangle = \cos(\theta/2) |0\rangle + e^{-i\phi} \sin(\theta/2) |1\rangle$ for generic $0 < \theta < \pi/2$ and ϕ. We have that

$$C_M \left(|\Theta\rangle^{\otimes N} \right) = N C_M \left(|\Theta\rangle \right), \tag{C4}$$

i.e. the magic capacity scales linearly with system size. This distinct scaling behavior clearly distinguishes typical and atypical states. Note that C_M is bounded as $C_M = O(N^2)$, where we find that the ground state of the Heisenberg model for $\Delta = 1$ satisfies such scaling.

Appendix D: Mutual von-Neumann SRE for MPS

We now show that the mutual von-Neumann SRE $\mathcal{I}_1^{[q]}(|\psi\rangle)$ can be efficiently computed with time $O(N\chi^3 \epsilon^{-2})$ for MPS

$$|\psi\rangle = \sum_{\{s_k\}} A_1^{s_1} \ldots A_N^{s_N} |s_1, \ldots, s_N\rangle, \tag{D1}$$

where A_k^s are matrices with maximal size $\chi \times \chi$. We assume two complementary bipartitions A and B. The 2-Rényi entanglement $S_2(\rho_A)$ and $S_2(\rho_B)$ can be efficiently computed for MPS via standard methods, where ρ_A, ρ_B are the reduced density matrix of the two bipartitions. Then, $\mathcal{I}_1^{[q]}(|\psi\rangle)$ can be computed as

$$\mathcal{I}_1^{[q]}(\rho) = \mathbb{E}_{P \sim q(P)} [\ln(\text{tr}(\rho P \rho P)) - \ln(\text{tr}(\rho_A P_A \rho_A P_A))$$
$$- \ln(\text{tr}(\rho_B P_B \rho_B P_B))] + S_2(\rho_A) + S_2(\rho_B)$$

where P_A and P_B are Pauli string P reduced onto subsystem A and B respectively, such that $P = P_A \otimes P_B$. Crucially, we need to sample from $q(P)$ which can be done in $O(N\chi^3)$ as shown in Ref. [17]. In particular, this can be done by ancestral sampling, using the following relation:

$$q(P) = q(P_1)q(P_2|P_1)\ldots q(P_N|P_1 \otimes P_2 \otimes \cdots \otimes P_N) \tag{D2}$$

where $P_i \in \{I, \sigma^x, \sigma^y, \sigma^z\}$ are single-qubit Pauli operators acting on the ith qubit and $q(P_2|P_1)$ conditional probabilities.

We start by computing the probabilities for the reduced density matrix $\rho_1 = \text{tr}_{2,\ldots N}(\rho)$ over the first qubit

$$q(P_1) = \sum_{P_2,\ldots,P_N} q(P_1, P_2, \ldots, P_N) = \frac{1}{2}\text{tr}(\rho_1 P_1 \rho_1 P_1) \tag{D3}$$

for all P_1. Here, we used the fact that after tracing out the kth qubit of ρ, the probability distribution over the reduced system can be written as

$$q_{\text{tr}_k(\rho)}(P) = \sum_{m=0}^{3} q_\rho(P \otimes P_k^m). \tag{D4}$$

We sample a Pauli operator P_1^* for the first qubit according to $q(P_1)$. Then, we proceed with the second qubit as

$$q(P_2|P_1^*) = \sum_{P_3,\ldots,P_N} q(P_1^*, P_2, \ldots, P_N)$$
$$= \frac{2^{-2}\text{tr}(\rho_{1,2}P_1^* \otimes P_2 \rho_{1,2}P_1^* \otimes P_2)}{2^{-1}\text{tr}(\rho_1 P_1^* \rho_1 P_1^*)}$$

where $\rho_{1,2}$ is the reduced density matrix of ρ over the first two qubits. Then, we sample a P_2 from $q(P_2|P_1^*)$. These steps are now repeated until N qubits are reached, finally gaining a Pauli $P \sim q_\rho(P)$. For improved efficiency, the MPS can first be brought to the left canonical form before performing the sampling procedure, as discussed in detail in Ref. [18]. After sampling P, one has to evaluate terms of the form $\text{tr}(\rho P \rho P)$ and $\text{tr}(\rho_A P_A \rho_A P_A)$, which can be done in $O(N\chi^3)$. In particular, the contractions for terms

$$\text{tr}(\rho_A P_1 \otimes P_2 \otimes \cdots \otimes P_{N_A} \rho_A P_1 \otimes P_2 \otimes \cdots \otimes P_{N_A}) \tag{D5}$$

with $\rho_A = \text{tr}_{\bar{A}}(\rho)$ can be done as shown in Fig. S4 with time complexity $O(N\chi^3)$ for MPS of bond dimension χ. Here, A_i denotes the tensor corresponding to the ith qubit of the MPS, P_i are the Pauli operator for the ith qubit, and lines are contracted over. For optimal complexity, one first contracts over the complement of subspace A, then the bonds that involve Pauli operators, and finally the remaining bonds.

Appendix E: Statevector simulation of Pauli sampling

We now show an improved statevector algorithm for Pauli sampling and Bell sampling. Here, by statevector simulation we mean that we describe the state by its full statevector amplitude $|\psi\rangle = \sum_i a_i |i\rangle$ which describes arbitrary quantum states. In contrast to naive sampling, which takes $O(8^N)$ time and $O(4^N)$ memory, our method requires only $O(8^{N/2})$ time and $O(2^N)$ memory. While MPS Pauli sampling in $O(N\chi^3)$ has the same asymptotic scaling (for worst case $\chi = 2^{N/2}$) [17, 18], we note that our algorithm directly works in the statevector representation of states, which is beneficial when working with states already given in statevector representation.

Note that our algorithm perfectly samples from the Pauli distribution directly, and does not use Monte-Carlo approaches to approximately sample. We apply our method to compute the von-Neumann SRE and magic capacity in Sec. F.
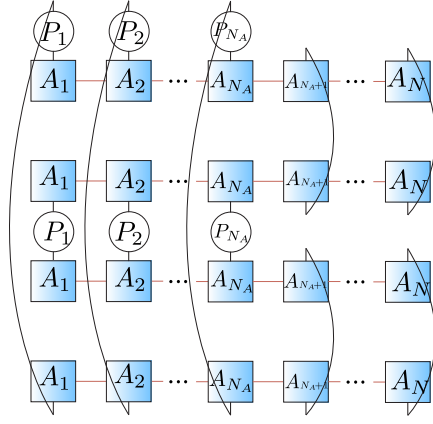
FIG. S4. MPS contraction to compute Eq. (D5).

First, we define the Pauli matrices $\sigma_{00} = I_2$, $\sigma_{01} = \sigma^x$, $\sigma_{10} = \sigma^z$ and $\sigma_{11} = \sigma^y$. The 4^N Pauli strings are N-qubit tensor products of Pauli matrices which we define as $\sigma_{\boldsymbol{n}} = \bigotimes_{j=1}^{N} \sigma_{\boldsymbol{n}_{2j-1}\boldsymbol{n}_{2j}}$ with $\boldsymbol{n} \in \{0,1\}^{2N}$. The Bell states are given by $|\sigma_{00}\rangle = \frac{1}{\sqrt{2}}(|00\rangle + |11\rangle)$, $|\sigma_{01}\rangle = \frac{1}{\sqrt{2}}(|00\rangle - |11\rangle)$, $|\sigma_{10}\rangle = \frac{1}{\sqrt{2}}(|01\rangle + |10\rangle)$ and $|\sigma_{11}\rangle = \frac{1}{\sqrt{2}}(|01\rangle - |10\rangle)$ and we define the product of Bell states $|\sigma_{\boldsymbol{r}}\rangle = |\sigma_{r_1 r_2}\rangle \otimes \cdots \otimes |\sigma_{r_{2N-1} r_{2N}}\rangle$.

We now want to sample from the probability distribution $p_{|\psi\rangle}(\sigma) = 2^{-N} \langle\psi|\sigma|\psi\rangle^2$. This can be done by sampling the Bell basis via [64, 70]

$$p(\sigma_{\boldsymbol{r}}) = 2^{-N} |\langle\psi|\sigma_{\boldsymbol{r}}|\psi\rangle|^2 = |\langle\boldsymbol{r}|\eta\rangle|^2, \tag{E1}$$

where $|\boldsymbol{r}\rangle$ is the computational basis state corresponding to bitstring $\boldsymbol{r}$. Here, we have the Bell transformed state $|\eta\rangle = U_{\mathrm{Bell}}^{\otimes N} |\psi^*\rangle \otimes |\psi\rangle$ with Bell transformation $U_{\mathrm{Bell}} = (H \otimes I_1)\mathrm{CNOT}$, where $H = \frac{1}{\sqrt{2}}(\sigma^x + \sigma^z)$ is the Hadamard gate, $\mathrm{CNOT} = \exp\left(i\frac{\pi}{4}(I_1 - \sigma^z) \otimes (I_1 - \sigma^x)\right)$ and $|\psi^*\rangle$ is the complex conjugate of $|\psi\rangle$. Thus, sampling $|\boldsymbol{r}\rangle$ in the computational basis from $|\eta\rangle$ is equivalent to sampling $\sigma_{\boldsymbol{r}}$ from $p(\sigma_{\boldsymbol{r}})$. However, storing the $2N$-qubit state $|\eta\rangle$ with the Hilbert space dimension of 4^N in memory is a major bottleneck.

To solve this problem, we provide a hybrid Schrödinger-Feynmann algorithm to sample $\sigma_{\boldsymbol{r}} \sim p(\sigma_{\boldsymbol{r}})$ which combines Bell and Feynmann-type approach for sampling for improved performance:

Theorem E.1 (Simulation of Pauli sampling in statevector representation). *Given an N-qubit state $|\psi\rangle = \sum_{i=1}^{2^N} a_i |i\rangle$, there is an algorithm to sample σ from the probability distribution $p(\sigma) = 2^{-N} |\langle\psi|\sigma|\psi\rangle|^2$ in $O(8^{N/2})$ time and $O(2^N)$ memory within the statevector representation of $|\psi\rangle$.*

Proof. The overall idea is to sample the first N qubits from $|\eta\rangle$ in a Feynmann-like algorithm, then switch to direct sampling with marginals for the last N qubits.

We start with the Feynmann-like part of our algorithm. Any N-qubit state $|\phi\rangle$ can be written as Schmidt-decomposition with $|\phi\rangle = a_0 |0\rangle |\phi_0\rangle + a_1 |1\rangle |\phi_1\rangle$, where $|0\rangle, |1\rangle$ are computational basis states and $|\phi_0\rangle, |\phi_1\rangle$ are normalized $N-1$ qubit states. For two copies, we have

$$|\phi^*\rangle |\phi\rangle = \sum_{k,q=1}^{2} a_k^* a_q |k\rangle |\phi_k^*\rangle |q\rangle |\phi_q\rangle \tag{E2}$$

We now reorder the positions of the qubits such that the first qubit of each copy are placed first. Then, we apply the Bell transformation U_{Bell} on the first qubit of each copy

$$|\eta'\rangle = U_{\mathrm{Bell}} \otimes I^{\otimes 2N-2} \sum_{k,q=1}^{2} a_k^* a_q |k\rangle |q\rangle |\phi_k^*\rangle |\phi_q\rangle = \tag{E3}$$

$$\frac{1}{\sqrt{2}} [|00\rangle (|a_0|^2 |\phi_0^*\rangle |\phi_0\rangle + |a_1|^2 |\phi_1^*\rangle |\phi_1\rangle) +$$

$$|01\rangle (a_0^* a_1 |\phi_0^*\rangle |\phi_1\rangle + a_1^* a_0 |\phi_1^*\rangle |\phi_0\rangle) +$$

$$|10\rangle (|a_0|^2 |\phi_0^*\rangle |\phi_0\rangle - |a_1|^2 |\phi_1^*\rangle |\phi_1\rangle) +$$

$$|11\rangle (a_0^* a_1 |\phi_0^*\rangle |\phi_1\rangle - a_1^* a_0 |\phi_1^*\rangle |\phi_0\rangle)]$$

We then measure the first two qubits $|nm\rangle$ in the computational basis with the probability

$$P(|nm\rangle) = \langle\eta'|\,(|nm\rangle\langle nm|\otimes I^{\otimes 2N-2})\,|\eta'\rangle\ .$$

As the tensor state $|\phi_n^*\rangle\,|\phi_m\rangle$ is too large to be stored directly in memory, we instead compute the sampling probabilities via the overlaps between the states $|\phi_n\rangle$ with the overlap matrix $E_{nm} = a_n^* a_m \langle\phi_n|\phi_m\rangle$. For example for outcome $|00\rangle$, we have

$$P(|00\rangle) = \frac{1}{2}(|E_{00}|^2 + E_{01}^* E_{10} + E_{10}^* E_{01} + |E_{11}|^2)$$

and the normalized projected state

$$|\eta_{00}\rangle = \frac{1}{\sqrt{2P(|0\rangle\,|0\rangle)}}(|a_0|^2\,|\phi_0^*\rangle\,|\phi_0\rangle + |a_1|^2\,|\phi_1^*\rangle\,|\phi_1\rangle) \tag{E4}$$

We now compute $P(|nm\rangle)$ and sample from it. After sampling, we gain two bits n, m which indicate the first Pauli operator σ_{nm} of the full Pauli string, as well as the normalized projected state $|\eta_{nm}\rangle$. Note that we do not store $|\eta_{nm}\rangle$ in memory directly, but only its amplitudes a_0, a_1 and the states $|\phi_0\rangle$, $|\phi_1\rangle$.

Starting with the projected state $|\eta_{nm}\rangle$, we can now repeat above steps to sample more qubits. For example, continuing with the example $|\eta_{00}\rangle$ of Eq. (E4), this state consists of two superposition states $|\phi_0^*\rangle\,|\phi_0\rangle$ and $|\phi_1^*\rangle\,|\phi_1\rangle$. On each superposition state, we repeat the step of Eq. (E3) and sample the next two qubits, gaining another two bits $k\ell$. Now, the projected state of $2N-4$ qubits $|\eta_{nmk\ell}\rangle$ is described by 4 superposition states. After k repetitions, we have sampled $2k$ bits $\boldsymbol{r}'$ which correspond to the Pauli operators for the first k qubits. The projected state $|\eta_{\boldsymbol{r}'}\rangle$ has $2N-2k$ qubits and is described by a superposition of 2^k states. After $k = N$ steps, we would have sampled the full Pauli string. The number of superposition state needed scales exponentially with k. Here, the main complexity arises from computing the overlap matrix E needed for sampling, which has $(2^k + 1)2^k/2$ non-trivial entries. The time complexity scales as $O(4^k 2^{N-k})$, while the memory consumption is $O(4^k)$.

If we were to continue sampling until the last qubits, there would be no advantage in terms of computational effort. However, we can reduce complexity by stopping early and doing only $k = N/2$ sampling steps, which has a complexity of $O(8^{N/2})$. At this point, the projected state of N qubits $|\eta_{\boldsymbol{r}'}\rangle$ is a superposition state of $2^{N/2}$ states. Note that the $2^{N/2}$ states that make up the superposition state take only $O(2^N)$ memory to store in total. After $k = N/2$ sampling steps, we switch to a direct sampling approach by explicitly constructing the state $|\eta_{\boldsymbol{r}'}\rangle$ of dimension 2^N by summing over the $2^{N/2}$ linear combinations of states with their corresponding coefficients. Constructing the state explicitly has a time complexity of $O(8^{N/2})$ and memory complexity $O(2^N)$. Then, we directly sample from $|\eta_r\rangle$ via its marginals in a time $O(2^N)$. This completes sampling of a Pauli string $\sigma_{\boldsymbol{r}}$ according to the probability distribution $p(\sigma_{\boldsymbol{r}})$. Our Bell sampling simulation runs in a time of $O(8^{N/2})$ and requires $O(2^N)$ memory. $\qquad\square$

In contrast to Pauli sampling (which is inefficient on quantum computers [83]) the closely related Bell sampling can be done efficiently in experiment. It samples from distribution $2^{-N}\langle\psi^*|\sigma|\psi\rangle^2$ [64] which can be sampled from via $U_{\text{Bell}}^{\otimes N}|\psi\rangle\otimes|\psi\rangle$. Our algorithm can also be used to perform Bell sampling. Here, one uses a modified Pauli sampling algorithm where one replaces the complex conjugate $|\psi^*\rangle$ at every step of the algorithm with the non-conjugated state $|\psi\rangle$.

Appendix F: Improved statevector computation of von-Neumann SRE and magic capacity

Now, we apply our Pauli sampling algorithm for statevector simulation to compute SREs and magic capacity. First, we want to compute the von-Neumann SRE

$$M_1(|\psi\rangle) = -\sum_{\sigma\in\mathcal{P}} p(\sigma)\ln\left(\langle\psi|\,\sigma\,|\psi\rangle^2\right) = -\mathop{\mathbb{E}}_{\sigma\sim p(\sigma)}[\ln\left(\langle\psi|\,\sigma\,|\psi\rangle^2\right)]\ . \tag{F1}$$

We perform Pauli sampling K times, gaining K Pauli strings $\{r_j\}_{j=1}^K$. From this, we compute the unbiased estimator of M_1

$$\hat{M}_1 = -\frac{1}{K}\sum_{j=1}^K \ln\left(\langle\psi|\,\sigma_{\boldsymbol{r}_j}\,|\psi\rangle^2\right)\ , \tag{F2}$$

where $\langle\psi|\,\sigma_{\boldsymbol{r}_j}\,|\psi\rangle^2$ can be evaluated in $O(2^N)$ time. The estimator has a variance

$$C_M = \mathrm{var}(\hat{M}_1) = \underset{P\sim p(P)}{\mathbb{E}}[\ln\left(\langle\psi|\,P\,|\psi\rangle^2\right)^2] - M_1^2 \tag{F3}$$

which is given by the magic capacity C_M. When averaging over K samples, the estimated mean value $\bar{M}_1$ has a standard deviation $\sqrt{C_M/K}$.

Now, we want to estimate the simulation complexity to achieve a given precision ϵ in the estimation of M_1. For this we need to bound the variance of our estimator given by $C_M = \mathrm{var}(\hat{M}_1)$. One can upper bound this via $\mathrm{var}(\ln\left(\langle\psi|\,\sigma\,|\psi\rangle^2\right)) \leq N^2 \ln(2)^2 + 1$ [18]. Thus, the estimation error ϵ of the average $\bar{M}_1$ scales in the worst case as

$$\epsilon \sim \sqrt{C_M/K} \sim \frac{N}{\sqrt{K}}\,. \tag{F4}$$

Note that to estimate the SRE density $m_1 = M_1/N$, we have similarly

$$\tilde{\epsilon} \propto \sqrt{C_M/(KN^2)} \sim \frac{1}{\sqrt{K}}\,. \tag{F5}$$

Overall, our algorithm scales as $O(8^{N/2}\epsilon^{-2})$ in time and $O(2^N)$ in memory, giving a square-root speedup over naive methods to compute SREs for statevectors. In particular, our method can compute the von-Neumann SRE of arbitrary states for 24 qubits using a standard notebook, while naive methods are limited to 15 qubits.

Appendix G: Critical point of TFIM via SREs and magic capacity

Here, we show how to determine the critical point from the SREs and magic capacity. The TFIM has a critical point at $h = 1$, where the ground state acquires universal behavior.

It has been shown that in the standard basis, the SRE M_2 can be used to determine the critical point [16]. Here, we use M_1, $\mathcal{I}_1$ and C_M to determine the critical point. In Fig. S5, we plot m_1, C_M/N and $\mathcal{I}_1^{[q]}$ against h for different N. Close to $h = 1$, we find that m_1 and $\mathcal{I}_1^{[q]}$ have a sharp peak, while C_M/N shows a minima. We record the extremal value and corresponding field h_0 for all N. Then, we fit $h_0(N)$ with $h_0(N) = -cN^{-\gamma} + h_c^{\mathrm{fit}}$ and use h_c^{fit} as approximation of the critical point. We find that m_1, C_M/N and $\mathcal{I}_1^{[q]}$ provide accurate estimations of the critical points.

Appendix H: Mutual SRE for basis-independent critical point of TFIM

A question raised by Ref.[16] was how to estimate the critical point h_{c} of the TFIM ground state via magic. It has been noted that in the standard basis, the magic of the ground state shows a clear universal peak at the critical point $h_{\mathrm{c}} = 1$. However, this is not true when one rotates the Hamiltonian into a different local basis via single-qubit unitaries V over all qubits N, i.e. $H' = V^{\otimes N} H V^{\otimes N\dagger}$. Then, in general, the magic of the ground state of the rotated Hamiltonian does not have a clear extremum at the critical point [16]. The critical point can be identified only by applying additional fitting procedures.

We now argue that the mutual SRE is a good indicator to find the critical point independent of the local basis.

First, in Fig.S6 we consider the standard local basis with the mutual 2-SRE $\mathcal{I}_2$ of the ground state of the TFIM as function of h. In Fig.S6a, we see that the mutual SRE for different N has a clear peak close to the critical point $h = 1$, where for increasing N the peak is approaching $h = 1$ asymptotically. Note that the peak is far more pronounced compared to just regarding SRE m_2. We see the convergence of the extremum to $h = 1$ with N more closely in Fig.S6b. In Fig.S6c, we plot $\mathcal{I}_2 - \mathcal{I}_2^0$, where subtract the maximal mutual SRE $\mathcal{I}_2^0$, against $(h - h_0)N$, where $h_0(N)$ is the field where we find the maximal mutual SRE for different N. We find that the rescaled curves collapse to a single curve close to the critical point. In Fig.S6d, we plot the minimal $h_0(N)$ against N. We fit with $h_0(N) = -cN^{(-\gamma)} + h_c^{\mathrm{fit}}$, where $h_0(N \to \infty) = h_c^{\mathrm{fit}}$ is the fitted critical field, which we show as dashed horizontal line. We find from the fit $h_c^{\mathrm{fit}} \approx 1.004$, which is close to the analytic value $h_{\mathrm{c}} = 1$.

Next, we study study the critical point for different local basis. We rotate $H' = V^{\otimes N} H V^{\otimes N\dagger}$ with local unitary V we choose from $V_\alpha(\theta) = \exp(-i\sigma^\alpha\theta/2)$, where σ^α is a Pauli matrix.
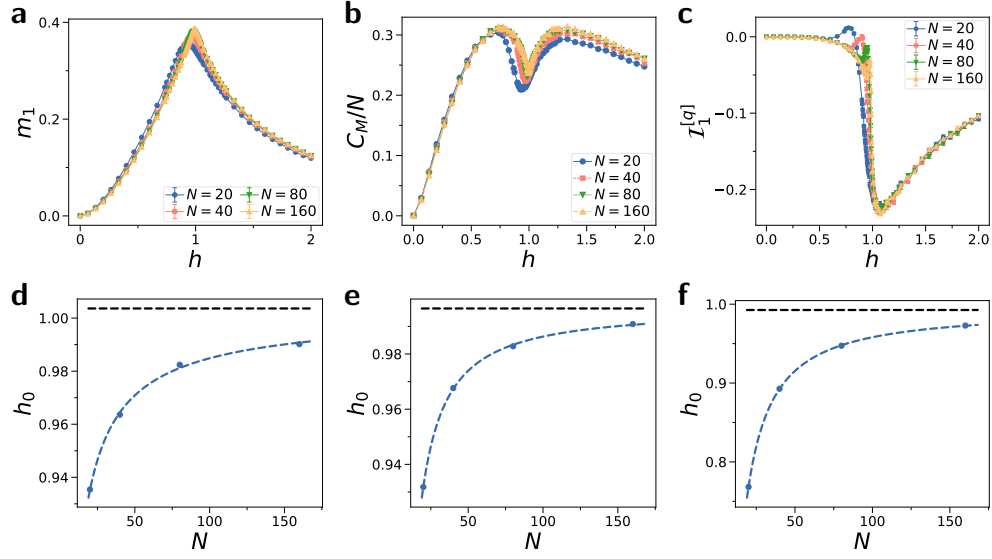
FIG. S5. Determining critical point h_c for groundstate of TFIM against field h, where we choose the Hamiltonian in the standard computational basis. We track the extremal value and the corresponding field $h_0(N)$ for different N. Then we fit $h_0(N)$ with polynomial $h_0(N) = -cN^{(}-\gamma) + h_c^{\text{fit}}$ to determine h_c^{fit}. **a)** $m_1 = M_1/N$, **b)** C_M/N and **c)** mutual von-Neumann SRE $\mathcal{I}_1^{[q]}$. Next, we plot $h_0(N)$ against N. We fit $h_0(N)$ with $h_0(N) = -cN^{-\gamma} + h_c^{\text{fit}}$, where corresponding fit h_c^{fit} as horizontal dashed line. We have **d)** m_1 with $h_c^{\text{fit}} \approx 1.0036$, **e)** C_M with $h_c^{\text{fit}} \approx 0.9965$, and **f)** $\mathcal{I}_1^{[q]}$ with $h_c^{\text{fit}} \approx 0.9926$.
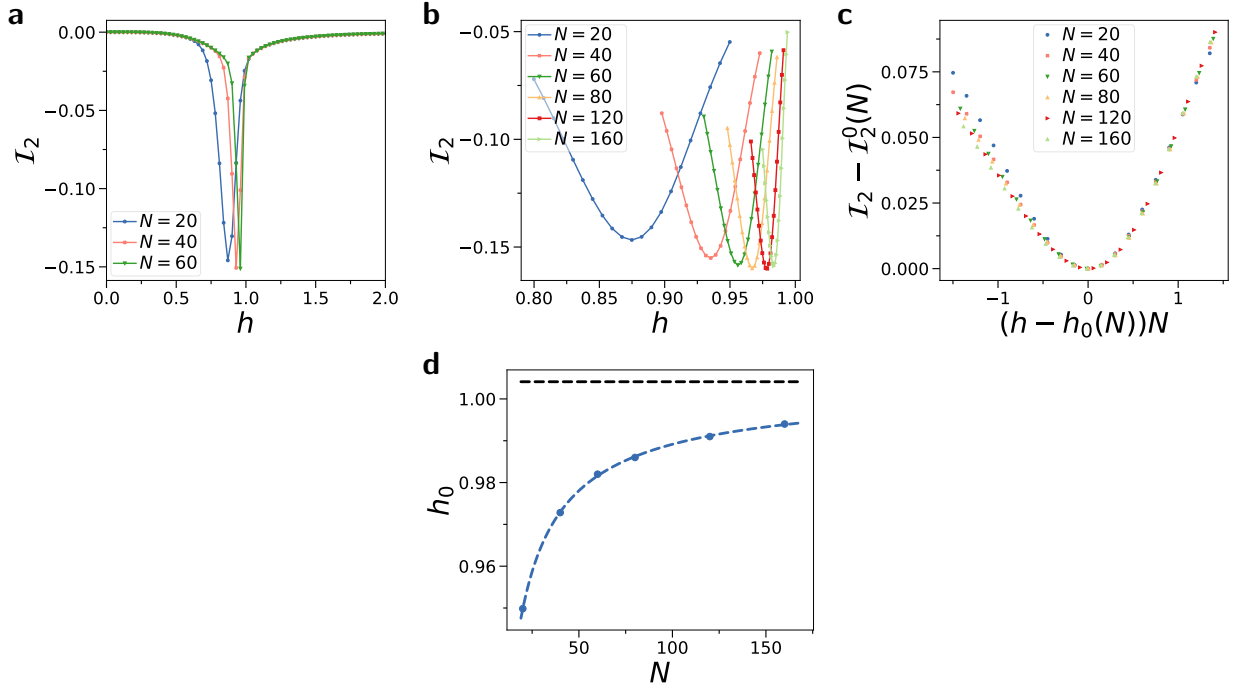

FIG. S6. Mutual 2-SRE $\mathcal{I}_2$ for equal bipartition of size $N/2$ close to criticality of the TFIM. **a)** $\mathcal{I}_2$ plotted against field h. **b)** $\mathcal{I}_2$ plotted against field h around critical point $h = 1$. **c)** $\mathcal{I}_2 - \mathcal{I}_2^0$ plotted against shifted field $h - h_0$ rescaled with N. We define $\mathcal{I}_2^0(N) = \max_h \mathcal{I}$ as the maximal mutual SRE over field h, which becomes maximal for $h_0(N)$. **d)** We plot $h_0(N)$ against N. We fit $h_0(N)$ with $h_0(N) = -cN^{-\gamma} + h_c^{\text{fit}}$, where $h_c^{\text{fit}} \approx 1.004$ is the fitted critical h_c for $N \to \infty$, which we show as horizontal dashed line.
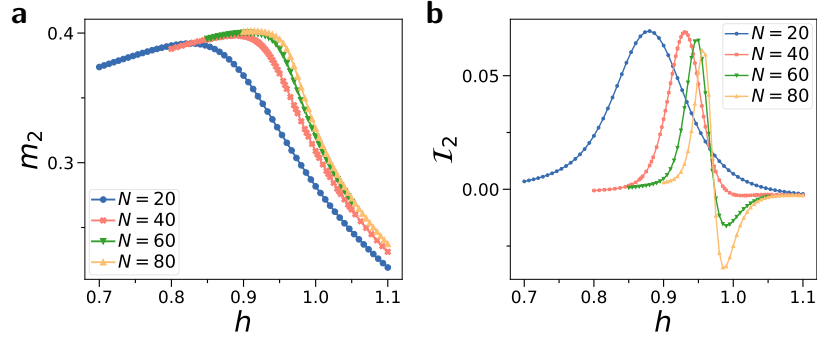
FIG. S7. Magic density m_2 and mutual 2-SRE $\mathcal{I}_2$ close to criticality of the TFIM in local basis rotated with single-qubit unitary $V_z(\theta) = \exp(-i\sigma^z\theta/2)$ with $\theta = \pi/4$. **a)** m_2 against h for $\chi = 10$. **b)** $\mathcal{I}_2$ with equal bipartition $N/2$ against h.

First, we study $V_z(\theta) = \exp(-i\sigma^z\theta/2)$ with $\theta = \pi/4$. We show m_2 in Fig. S7a, finding the absence of an extremum at $h = 1$. In contrast, we find in Fig. S7b that $\mathcal{I}_2$ is clearly peaked towards $h = 1$, where we find a minimum that converges towards $h = 1$ large N.

This feature is independent of the local basis. For m_2 depending on the chosen local basis V there is no clear peak towards $h = 1$ as seen in Fig. S8a (for detailed study see Ref. [16]). In contrast, $\mathcal{I}_2$ has a clear extremum that converges towards $h = 1$ for large N as seen in Fig. S8b.
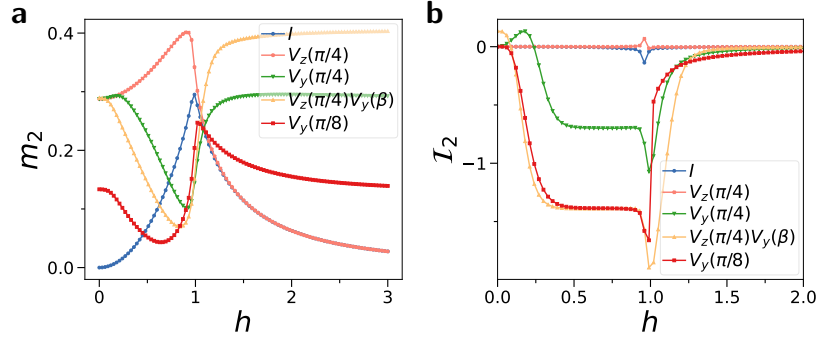

FIG. S8. Magic density m_2 and mutual 2-SRE $\mathcal{I}_2$ close to criticality of the TFIM in various local basis V. Here, $\beta = \arccos(1/\sqrt{3})$ which transforms into the basis of maximal single-qubit magic. **a)** m_2 for various different local basis against h with $N = 80$ and $\chi = 6$. **b)** $\mathcal{I}_2$ for various different local basis against h with $N = 80$ and $\chi = 6$.

Finally, we note that the mutual von-Neumann SRE $\mathcal{I}_1^{[q]}$ can also be used as basis-independent indicator of the critical point. In Fig. S9, we show von-Neumann SRE density m_1 (Fig. S9a), the magic capacity C_M (Fig. S9b) and $\mathcal{I}_1^{[q]}$ (Fig. S9c) for different rotated basis. In Fig. S9c, We observe a distinct sharp peak for $\mathcal{I}_1^{[q]}$ close to the critical point $h = 1$ for all chosen basis, which can serve to characterize the critical point by a scaling analysis.
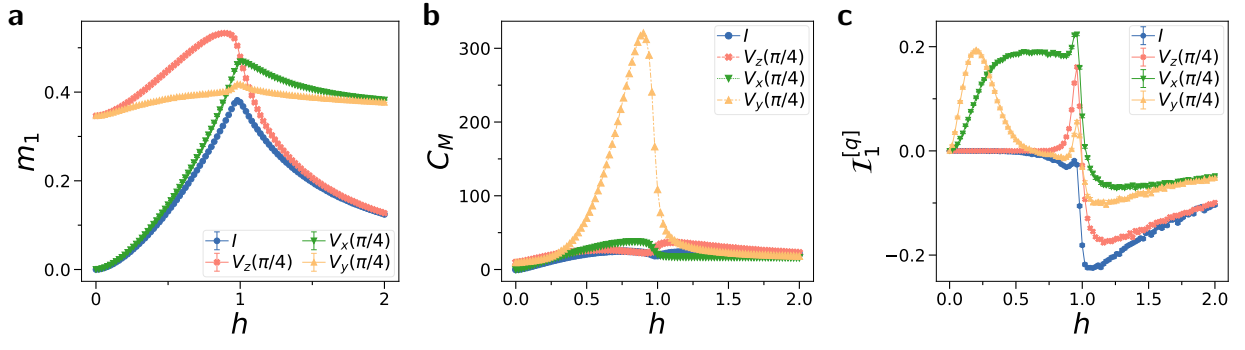
FIG. S9. Magic of groundstate of TFIM against field h for different basis V_α. **a)** Von-Neumann magic density m_1 **b)** Magic capacity C_M **c)** Mutual von-Neumann SRE $\mathcal{I}_1^{[q]}$. We have $N = 80$ qubits and $K = 10^5$ Pauli samples.